HYDROCOASTAL - RACZIW

SAR/SARin Radar Altimetry for Coastal Zone and Inland Water Level

Processors case studies report
WP3110, WP3120 and WP3130
Deliverable D2.7

Sentinel-3 and Cryosat SAR/SARin Radar Altimetry for Coastal Zone and Inland Water

ESA Contract 4000129872/20/I-DT

Project reference: HYDROCOASTAL_ESA_ARESYS_TN_D2.7
Issue: 1.0

This page has been intentionally left blank

Change Record

Date	Issue	Section	Page	Comment
31/05/2023	1.0			First Issue

Control Document

Process	Name	Date
Written by:	Aresys	31/05/2023
Checked by		
Approved by:		

Subject	Radar Altimetry for Coastal Zone and Inland Water Level	Project	HYDROCOASTAL - RACZIW

Author	Organisation	Internal references
Lisa Recchia	Aresys	
Pietro Guccione	Aresys	
Davide Giudici	Aresys	

	Signature	Date
For HYDROCOASTAL team		
For ESA		

Table of Contents

List of Acronyms

CS2	CryoSat-2
D/D	Delay/Doppler
DEM	Digital Elevation Model
FBR	Full Bit Rate
FFSAR	Fully Focused SAR
UF-SAR	UnFocused SAR
IRF	Impulse Response Function
L1B	Level 1B Product
L1BS	Level a1 Stack Product
OCOG	Offset Centre Of Gravity
POCA	Point Of Closest Approach
PRF	Pulse Repetition Frequency
SAR	Synthetic Aperture Radar
SARin	SAR Interferometric mode
SLC	Single Look Complex
SSH	Sea Surface Height
SWH	Significant Wave Height
S3	Sentinel-3
S6	Sentinel-6
WHS	Water Surface Height

1 Introduction

1.1 The HYDROCOASTAL Project

The HYDROCOASTAL project is a project funded under the ESA EO Science for Society Programme, and aims to maximise the exploitation of SAR and SARin altimeter measurements in the coastal zone and inland waters, by evaluating and implementing new approaches to process SAR and SARin data from CryoSat-2, and SAR altimeter data from Sentinel-3A and Sentinel-3B.

One of the key objectives is to link together and better understand the interactions processes between river discharge and coastal sea level. Key outputs are global coastal zone and river discharge data sets, and assessments of these products in terms of their scientific impact.

1.2 Scope of this Technical Note

The scope of this technical note is is outcome of the analysis of the Processing Case Studies carried out by Aresys in the framework of WP3100, i.e.

- WP3110: FFSAR
- WP3120: Attitude Errors
- WP3130: Along/Across track slope

1.3 Reference Documents

RD-01 RACZIW Technical Proposal, SatOC and RACZIW team, May 2020.

1.4 Document Organisation

After this introductory section, Section 2 provides an overview of the results for the FFSAR in frequency domain case study while Section 3 and Section 4 provide a summary of the results obtained for the Attitude and Along/Across-track slope errors analysis.

2 Processing Case Studies: FFSAR

This section describes the results obtained from the Processors Case studies carried out by Aresys in the framework of WP3110: FFSAR.

2.1 FFSAR Processing in frequency domain

The full focusing of radar altimeter data is a new concept recently proposed by Egido and Smith in [Egido et al., 2017]. Actually, the possibility of focusing nadir-looking altimeter echoes for a longer illumination time than the extent of a burst was firstly suggested in [Raney, 2014], where it was underlined that even if the Delay/Doppler (D/D) mode was renamed “SAR Mode” it actually is an unfocused Synthetic Aperture Radar processing, since focused SAR processing would require an azimuth matched filter to coherently sum more bursts together.

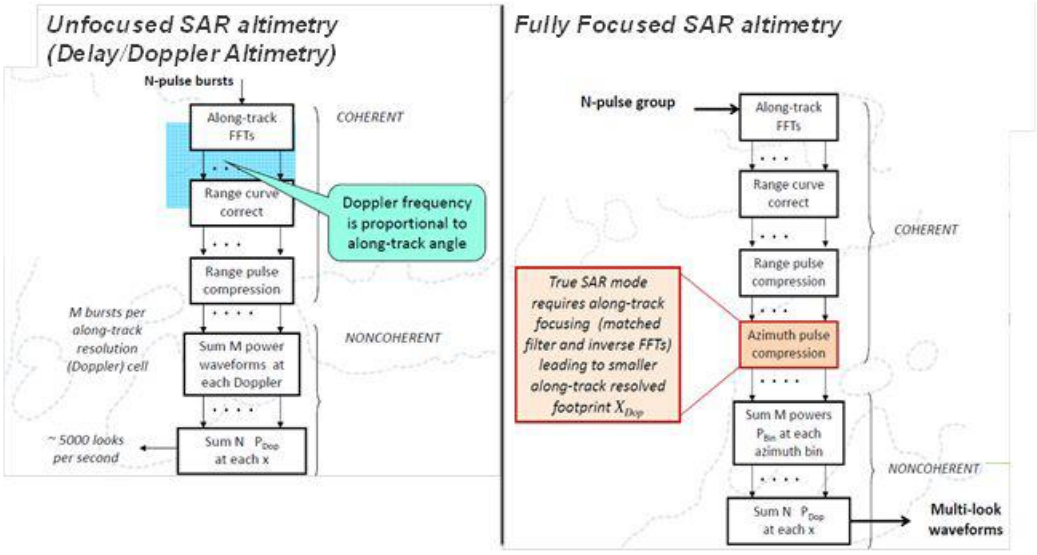

Figure 1. Delay/Doppler and Fully Focused SAR processing chains.

Under the assumption that the instrument maintains the signal coherency by, at least, a full illumination time, it is possible to complete the processing chain of a D/D altimeter by making focusing in the along-track too, over the entire illumination time of a scatterer on the surface. In [Egido et al., 2017], the proposed FF SAR algorithm aims basically at the progressive compensation of the different phase terms in the impulse response function, similarly to what is done in the back-projection algorithm for side-looking SAR imaging systems. Fully focused back-projection algorithm has shown to be a robust

way to focus altimeter data, at least in close burst configuration. However, the processing is quite cumbersome, because each ground output sample requires ad-hoc correction of the phase terms of the IRF (which is a function of the relative distance sensor-target and so of the local geometry), i.e. the back-projection is output dependent. This means that the main processing steps (range migration correction, range compression, residual video phase compensation and relative range phase compensation) need to be repeated for each along track output position. Aresys already investigated on focusing algorithms in frequency domain for high PRF radar altimeters that are alternative with respect to the back-projection algorithm. Focusing algorithms in frequency domain have been proved to be computationally at least 450 times less expensive than back-projection while preserving a good quality of the IRF, as discussed in [Guccione et al., 2018]. The block scheme of the WK FFSAR algorithm is shown in the following figure (Figure 2).

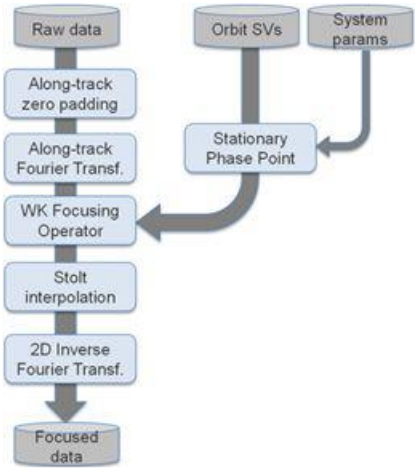

Figure 2. WK FF SAR in frequency-domain: block scheme.

Around the WK FFSAR processor, Aresys developed a Generic FFSAR processing chain to process L1A (or FBR) products up to L1b products. A high-level view of the Generic FFSAR processing chain is given in the following figure (Figure 3).

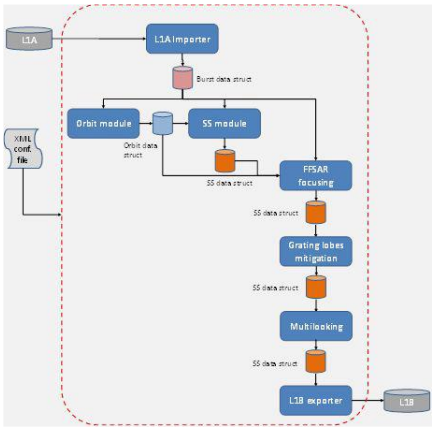

Figure 3. Generic FF SAR processing chain

Aresys has exploited the in-house Generic FFSAR processing chain in the frequency domain to obtain multi-looked L1b products containing FFSAR waveforms. In the following sections the outcomes of the investigation on two different topics are presented:

- In Section 2.2 the multi-looking step is investigated to trade-off between the along-track sampling of the waveforms and the speckle reduction, which is particularly of interest in the coastal zone.
- In Section 2.3 an overview on the issue of the grating lobes affecting FFSAR waveforms is provided. This effect is particularly visible on inland bodies. A study is performed to assess different strategies for the grating-lobes mitigation.

2.2 Multilooking rate analysis

The main interest of multi-looking is to reduce the Gaussian distributed speckle noise to have a better geophysical parameter identification during the waveform retracking. FF-SAR multilooking is a spatial averaging, contrary to look angle multi-looking of UF-SAR, meaning that consecutive single- looks are averaged together to reduce the noise. Such multi-looking is at the expense of the along-track resolution, which need to be preserved as much as possible.

A starting point trade-off between resolution and noise reduction is usually found out roughly by visual observation of the waveforms. From this, it comes out the desire to set up a procedure to define the posting rate. In practice:

- A high posting rate means higher resolution, but lesser single waveforms averaged together

and then, higher noise level.

A low posting rate means more single waveforms averaged together (i.e., lower noise level) but less resolution.

For the sake of formalism, let us consider successive single-look FF-SAR waveforms s_i with speckle noise following any random distribution with the same zero mean value, standard deviation $\sigma > 0$ and covariance factor $\rho \in [-1,1]$. Single-looks are independent when $\rho = 0$; when $\rho > 0$ they are correlated and in the special case when $\rho < 0$ they are negatively correlated. Let us consider the special case where the correlation factor between single-looks follow an exponential decaying law:

$$cov(s_i, s_j) = \sigma^2 \rho^{|j-i|} \quad \text{Eq. 1.}$$

The previous equation arbitrarily models the effect of speckle decorrelation with spatial distance using an exponential decaying law. After multilooking, the variance is diminishing as follows:

$$\sigma_n^2 = var\left(\sum_i |s_i|^2\right) = \sigma^2 \cdot \left(\frac{1}{n} + \frac{2\rho}{n^2} \cdot \frac{n\rho - n + 1 - \rho^n}{2\rho - \rho^2 - 1}\right) \quad \text{Eq. 2.}$$

being n the number of SLC waveforms averaged together. The optimal multi-looking factor corresponds to the number of single-looks to be averaged to reach a variance below a certain threshold.

To understand this trade-off, the theoretical trend of the standard deviation reduction as a function of the number of samples averaged together has been analyzed. In the figure below, two cases have been reported.

1. The trend of the completely independent waveforms. This trend can be achieved by setting $\rho = 0$ in Eq. 2. In this case we have $\sigma_n = \sigma/\sqrt{n}$ (it corresponds to the dotted black line in the figure 2.4).
2. The exponential decaying low is assumed for the correlation between the SLC waveforms.

Using Eq. 2, σ_n has been evaluated with a $\rho = 0.5$. This case corresponds to the green line in the figure 4.

Finally, the blue line corresponds to the real trend of the noise standard deviation reduction when progressively, more and more waveforms are average together. As can be seen, the exponential decaying function better fit the real trend of the noise waveforms.

This confirms that the model in Eq. 2 can be used to understand the trend of the reduction of the standard deviation of the noise waveforms when averaged together. The robustness of the model is analyzed in Fig 2.5, where two different cases of ocean waveforms have been plotted w.r.t. the model of Eq. 2 and still using a $\rho = 0.5$. As can be seen, the difference between SWH=2m and SWH=4m from the noise reduction trend point of view is minimal.

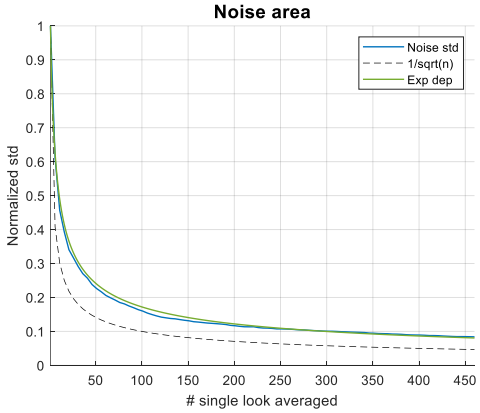

Figure 4. Relation between theoretical noise reduction and real data behavior.

To practically exploit the plot, let us suppose we aim at reaching 80% of decrease of the noise standard deviation (black horizontal dotted line). The cross between the horizontal line and the curves provides, on the horizontal axis, the number of single looks to average together to get such noise reduction.

In the special case where the single looks are fully independent (i.e. $\rho = 0$) the variance decreases of a factor of 1/n (the black solid line in Figure below) and the required SLC waveforms to average are below 50. Instead, when correlation is present (i.e. $\rho \in]0,1]$), the variance decreases a littlebit slower and more waveforms are needed. Figure 2.5 shows that multi-looking depends only slightly on SWH. For SWH of 4m a posting rate of 140hz need to be used compared to 151hz for SWH of 2m.

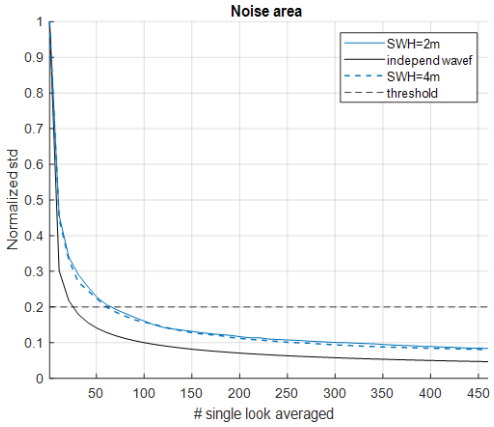

Figure 5. Behavior of two real data cases: To achieve a noise reduction of 80%, a posting rate of 151hz need to be employed for SWH about 2m (blue solid line) and a posting rate of 140hz for SWH about 4m (blue dashed line). It corresponds to 60 and 65 single-looks averaged respectively.

Notably, the example presented in the figure deals with real data acquired over ocean. In proximity of coastal zones, the leading edge of the waveforms are expected to have more energy, with part of this energy leaking in the noise area, due to the finite extent of the acquiring window. However, this effect is contained, and we can safely suppose that the trend of the normalized standard deviation w.r.t. the number of averaged waveforms reported in the figure above does not basically change. Most likely, an adjustment of the factor ρ is required to better fit real data and the model.

In summary, the previous plot and the mathematical model can be used as a reference to decide the trade-off between the percentage of noise standard deviation to be reduced and the final resolution of the multilook product.

A comparison between the radargram of a Sentinel-3 product is reported in the figure below for two different cases of multilook averaging. As expected, the radargram in Fig. 6 is “smoother” (i.e. averaged) but less resoluted than the one in Fig. 7 (example, see in the area around 63.55deg of latitude).

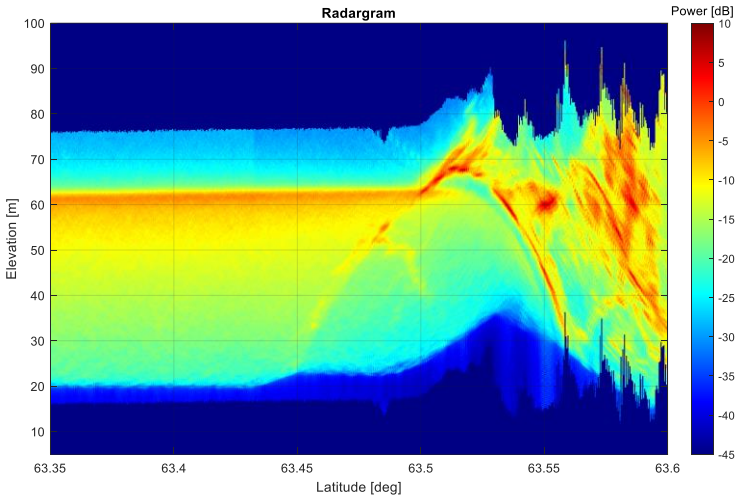

Figure 6. Sentinel-3 dataset 20170526T212449. The area corresponds to the north coast of Iceland. Multilook used: 150Hz

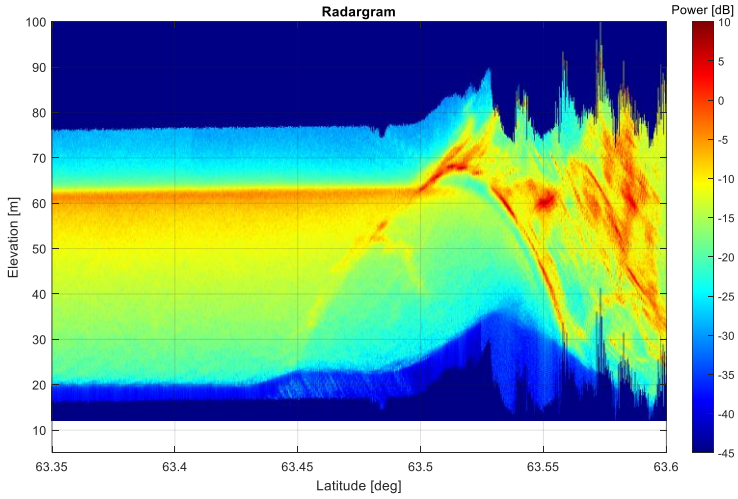

Figure 7. Sentinel-3 dataset 20170526T212449. The area corresponds to the north coast of Iceland. Multilook used: 500Hz

2.3 Grating lobes mitigation

When data are acquired in closed-burst configuration, as occurs for Cryosat and Sentinel-3, the chronogram χ is modelled in amplitude [Guccione et al., 2018] as a succession of rectangle functions. Said $h(\eta, t)$ the impulse response of an equivalent open-burst acquisition system, the

corresponding close-burst acquisition is expressed by:

$$\chi_{cb}(\eta, t) = h(\eta, t) \cdot \sum_{n} rect\left(\frac{\eta - nT_p}{T_B}\right) \quad \text{Eq. 3.}$$

In the previous expression, η is the along-track time, t is the fast time (across-track), $T_p = 1/BRF$ is the burst repetition time while $T_B = N_b/PRF$ is the burst duration, with N_b the number of pulses in a burst. In the previous expression, the antenna pattern has not been included.

The Doppler spectrum of a closed-burst acquisition presents a similar behavior: the continuous antenna-shaped spectrum is cut by a series of rectangle functions in frequency:

$$X_{cb}(f_a, t) \approx G_{al}\left(\frac{f_a}{f_R}\right) \cdot \exp(j\Phi(f_a, t)) \cdot \sum_{k} rect\left(\frac{f_a - kW_p}{W_b}\right) \quad \text{Eq. 4.}$$

In the previous expression, $W_p = |f_R|T_p$ is the distance between the successive rectangular pulses while $W_b = |f_R|T_b$ is the extension of them. The quantity $f_R = -\frac{2v_{eq}^2}{\lambda R_0}$ is the Doppler rate, i.e. the derivative of the instantaneous Doppler frequency. Apart for the phase term $\Phi(f_a, t)$, that must be properly compensated during the along-track focusing, the amplitude of the spectrum is shaped by the antenna pattern.

To provide a visual example of the previous expression, the Cryosat spectrum, achieved by simulating a point target, is reported in Figure 8 (left panel) together with a zoom on the repeated pulses pattern (right panel).

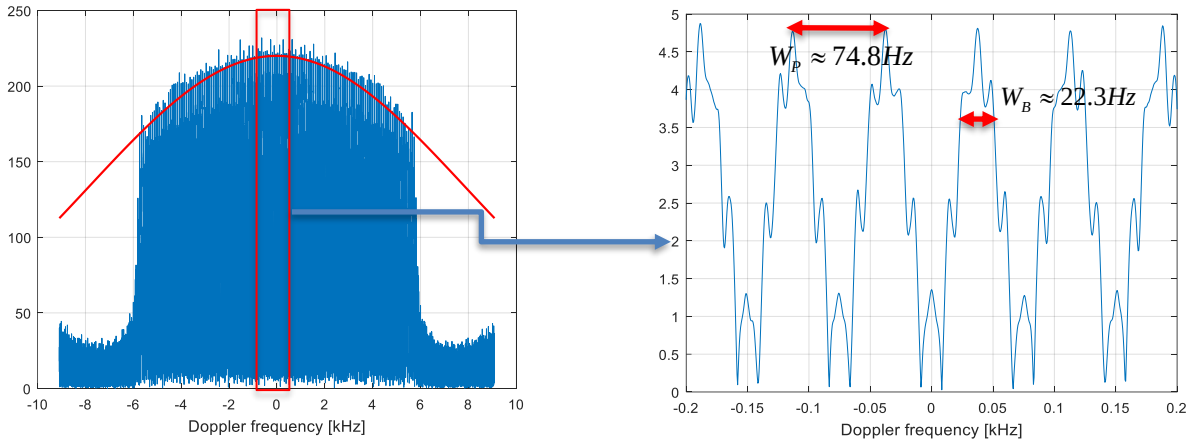

(a) (b)

Figure 8. Doppler spectrum of a simulated point target. (a) Whole Doppler spectrum (blue) with the antenna shape superimposed (red); (b) detail around 0Hz: strips of band W_b and distant W_p can be seen.

The focused IRF is achieved after the compensation of the phase term $\exp(j\Phi(f_a,t))$ in Eq. 4 and is the usual $sinc(B_d\eta)$, with $B_d = |f_R|T_b$ the Doppler bandwidth, repeated at step $1/W_p$ and shaped by the along-track antenna pattern and the inverse transform of the single rectangle function of the series, i.e. $sinc(W_b\eta)$. The final expression is:

$$y_{cb}(\eta,t) = G_{al}(\eta)\cdot sinc(W_b\eta)\cdot\sum_n sinc\left(B_d\left(\eta-\frac{n}{W_p}\right)\right) \quad \text{Eq. 5.}$$

The repetition of the sinc impulses, mitigated by the antenna pattern and by the $sinc(W_b\eta)$ are the well-known grating-lobes effect, which occurs for closed-burst acquisition only. Grating lobes in the focused time domain correspond to a series IRF periodically repeated at a distance $\Delta y_{gr} = v_{gr}/W_p$.

In the table below, the typical quantities involved in the grating lobes effect are reported for the two sensors.

Sensor	T_b **[ms]**	T_p **[ms]**	W_b **[Hz]**	W_p **[Hz]**	f_R **[Hz/s]**	Δy_{gr} **[m]**
Cryosat	3.520	11.793	22.54	75.52	-6403	89.6

Sentinel-3	3.590	12.734	19.64	69.66	-5471	95.5

The grating lobes effect can be better visualized and investigated on a single simulated point target or transponder since both the cases correspond to isolated and under-control targets. In Figure 9, it is reported the amount of grating lobes for a simulated point target and using Cryosat typical parameters. Along-track antenna pattern has been compensated. Nominally, the first grating lobe has a level of about -9dB w.r.t. the main target amplitude. However, the successive grating lobes have a level that is lower than what expected, i.e. the red-dotted antenna pattern envelope. In fact, considering some recent work [Ray et al., 2015, Ehlers et al., 2022], we know that the grating lobe is a two-dimensional problem (along and across track), and replicas contaminate different range gates due to a smearing effect, i.e. due to the fact that the focusing operator is not exact for them and, then, they are defocused.

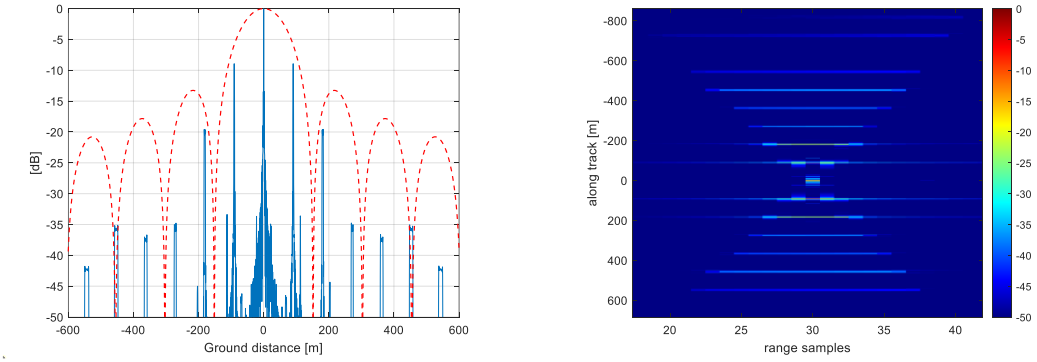

(a) (b)

Figure 9. Visualization of the grating lobes for a simulated point target. Cryosat parameters used. (a) along-track cut in the target position; (b) 2D point target power

In real datasets, the grating lobes are particularly visible on hydrology and sea-ice areas since on these heterogenous surfaces the difference in amplitude (image dynamics) can be high.
Figure 10 shows the effect of grating lobes for an acquisition taken by Sentinel-3 in the southern coast of Iceland. The grating lobes of a strong target are well visible in the sea area at the expected distance.

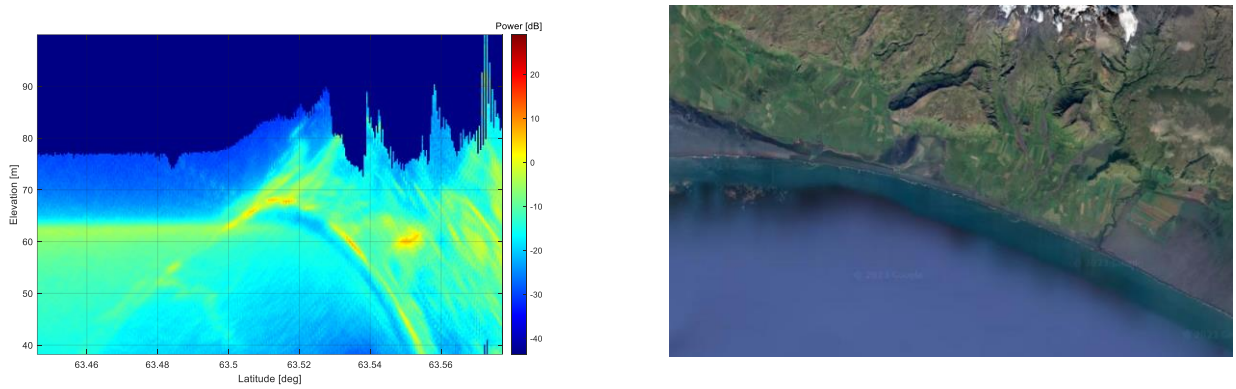

(a) (b)

Figure 10: Grating lobes in Sentinel-3. Acquisition 20170526T212449 in region [63-63.8]° of latitude (southern coast of Iceland). (a) Radargram. Groups of grating lobes are visible at latitude 63.515°. (b) Corresponding region (credits: Google Earth). An inland water area is visible near the shoreline, about at the center of the image.

Notably, the problem is present even in the case of Sentinel-6 as a parabola (see the radargram in Figure 11 representing inland water acquisition). Sentinel-6, although considered an open burst altimeter, it is formally a closed-burst on a synthetic aperture since the burst of 64 pulses are alternated to two pulses of calibration (so, in S-6 case, T_p and T_b are close). For Sentinel-6 case, the first replica is -33dB lower than the main lobe but it is still visible in acquisitions with large dynamics.

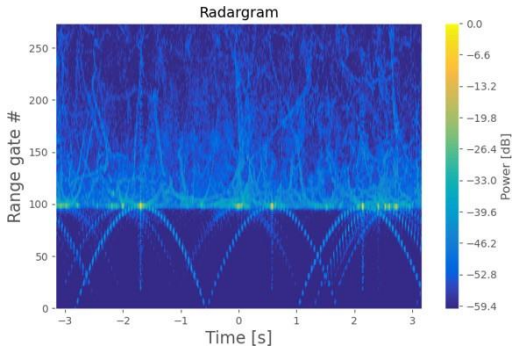

(a) FF-SAR radargram

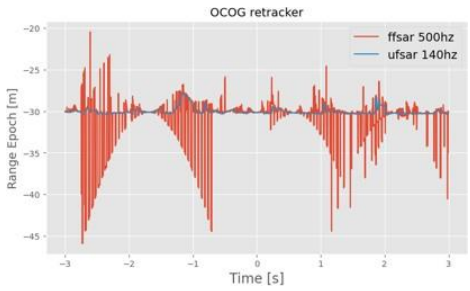

(b) OGOC retracker epoch point

Figure 11.: Effect of replicas over sea-ice lead surface. (a) Replicas have a parabola shape signature on the fully-focused radargram. This can lead to huge differences of several meters in the estimation of the water surface height compared to unfocused (b). The retracker does not distinguish replicas from the real surface signal.

In the inland water regions, the grating lobes are particularly harmful for the estimation of water surface height (WSH). The retracker is easily trapped by replicas on the thermal noise area where no signal is yet received, leading to error in WSH of tens of meters. All types of retracker show the same issue: empirical retracker (OCOG) but also optimal retrackers (such as sinc squared) have been tested. Replicas of this type are particularly harmful for the estimation of water surface height (WSH).

Replica mitigation

We underline again that this impairment is part of the physics of the acquisition system and cannot be avoided. Basically, it corresponds to lack of energy in the full B_d-wide spectrum. So, it cannot be avoided using some spectrum shaping or reduction as in the open-burst acquisitions. In Sentinel-6, which is an open-burst altimeter, the spectrum is basically flat and the very-low grating lobes (around -33dB below the main lobe level) are present because of the 2 calibration pulses after the 64 pulses of the burst during acquisition. This reflects in a spectrum which is basically smooth in the main region with light undulation at edges. Removing or re-shaping the spectrum may work in some reduction of the already low replicas, at the expense of the along-track resolution.

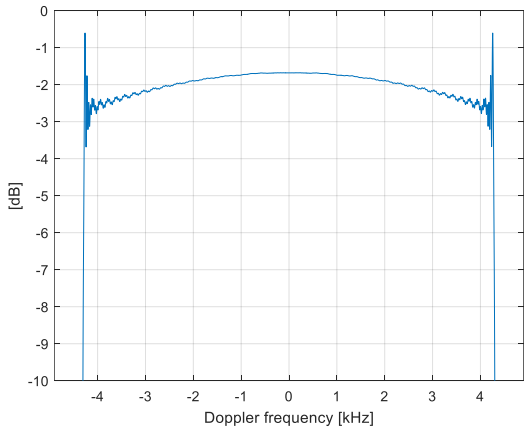

Figure 12.: Sentinel-6 spectrum from a simulated point target.

In the closed-burst acquisition, heavy undulations throughout the spectrum are visible (see Figure 8) and a spectrum reduction would not work in reduction of grating lobes. It is worth to note here that Cryosat-2 and Sentinel-3 have been designed to work over not specular targets. So, the grating lobes are an impairment due to the “improper” use of such sensors over regions different from the ones originally considered in the design.

Anyway, some methods to mitigate the grating lobes can be adopted. In Figure 13, it is reported a block scheme of the replica mitigation that could be adopted to reduce the strongest target grating lobes.

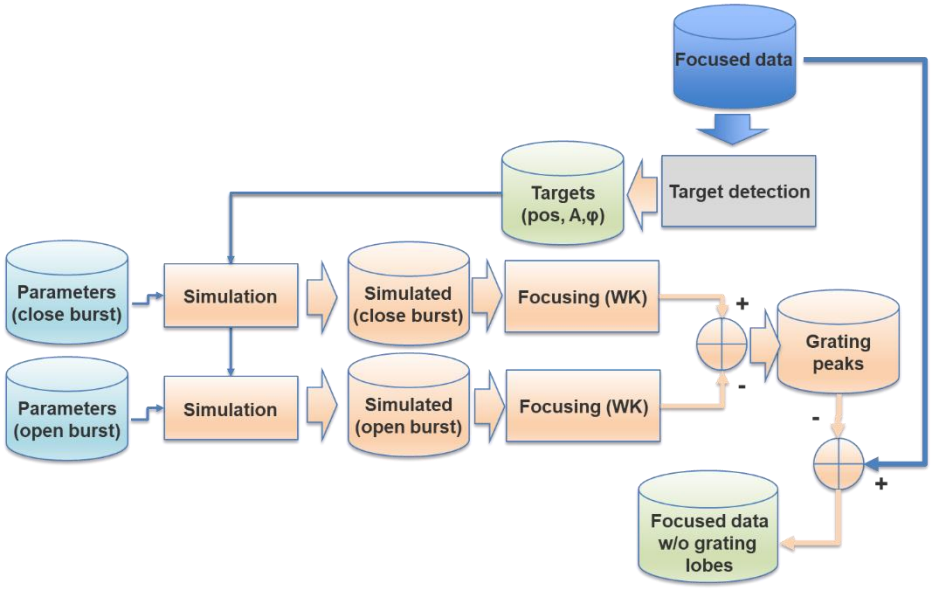

Figure 13.: Block scheme of the grating lobes

The idea is to use a simulation to replicate the point target behavior if they were acquired using an open and a close burst configurations (the two branches in parallel in the scheme). After focusing, for each point target, the two branches have a focused target with and without grating lobes, due to the close and open burst simulated acquisitions, respectively. The difference between the two would provide only the grating lobes energy for the exact location of each targets. The grating lobes can be, finally, subtracted from the original image to remove the replicas. The scheme works well in two conditions: (i) strong point targets are not too much overlapped each other, i.e. they are a reasonable number within the image; (ii) a method to identify them must be provided to the algorithm (grey block in the scheme).

Using a simple simulation with Cryosat parameters, this scheme has been applied to a simulated image with few numbers of point targets. Results are in Table below.

TARG	ALONG POS	ACROSS POS	A [DB]	Φ [DB]	EST A [DB]	EST Φ [RAD]	GRATING LOBE LEVEL [DB] - REL
1	0	0	0	0	0.076	-0.002	-49.50
2	1247	27	6.522	-0.337	6.556	-0.336	-54.60
3	3450	-7	0.645	-0.381	0.751	0.382	-51.25
4	124	24	2.577	2.409	2.612	-2.406	-52.41
5	4780	31	-0.132	1.153	-0.108	-1.147	-46.05
6	-499	37	12.889	-0.995	12.905	1.003	-48.81

Six point targets have been set in a simulated image with random value of amplitude and phase. The method described in Figure 13 has been used to mitigate the grating lobe level. Estimated amplitude and phase and strongest grating lobe level after mitigation are reported in the Table. To better provide an illustration of the method, in Figure 14 a visual impact of the grating lobes mitigation is reported.

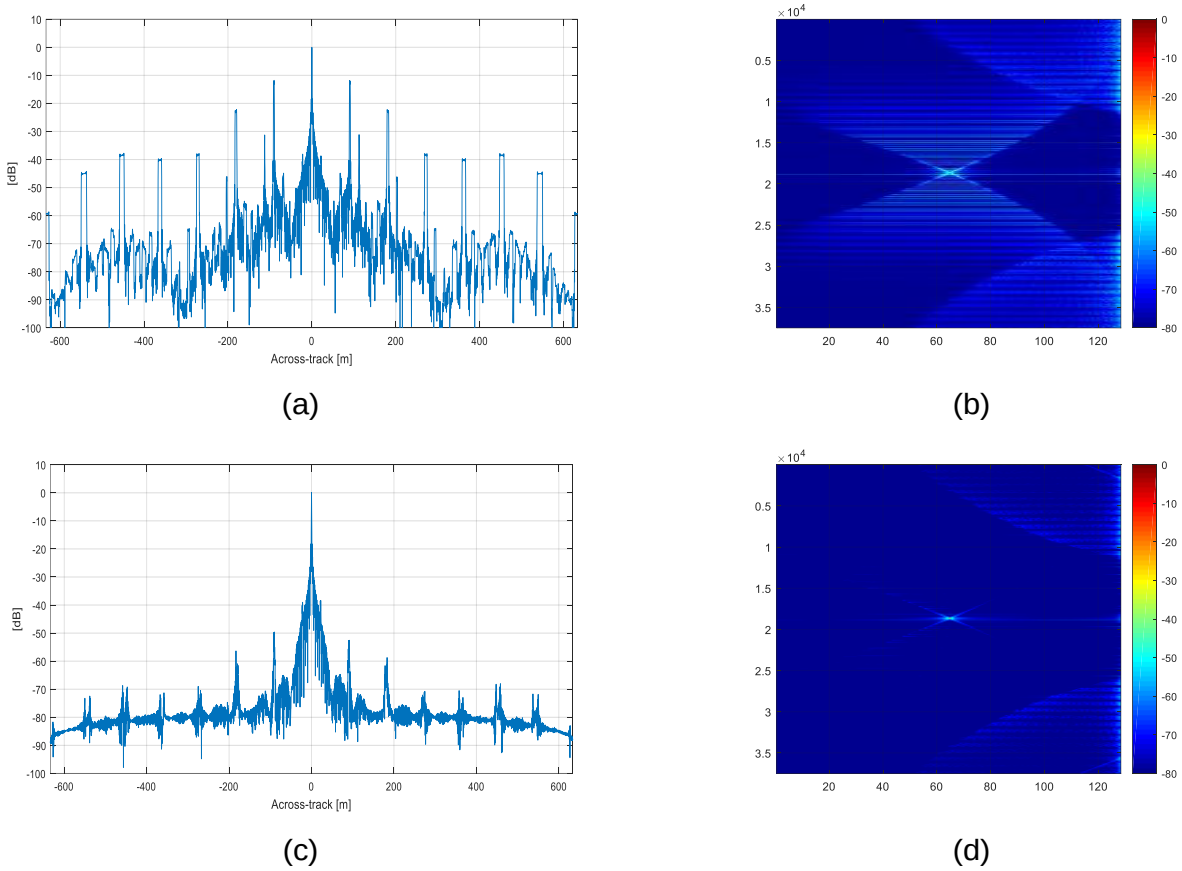

Figure 14.: Visual impact of the application of the method proposed for grating lobes mitigation. (a): azimuth cut of the point target shown in (b) in the 2D image. (c) Azimuth cut of the same point target after mitigation and (d) the 2D image.

The method is still in a prototype version and should be properly refined and tested over real images to understand the true applicability.

3 Processing Case Studies: Attitude errors

This section describes the results obtained from the Processors Case studies carried out by Aresys in the framework of WP3120: Attitude Errors.

Precise attitude information is crucial for altimetry. In fact, the analytical models for pulse-limited echoes that are operationally exploited to retrieve measurements of the sea state are functions of the satellite pointing so that, independently of the along-track and the across-track mispointing, a similar effect on the returned echoes is obtained. As a consequence, any error in the knowledge of satellite pointing can affect the accuracy of the estimated measurements, depending on the adopted altimeter waveform retracker. Similar considerations apply to SAR altimetry, whose echoes have been modelled analytically as functions also of satellite pointing. Moreover, it has been shown that the along-track mispointing affects the amplitude of the multi-looked echoes, so a priori knowledge of the along-track mispointing is needed to correctly retrieve the amplitude of the waveform. Aresys has assessed the attitude errors by exploiting the following approaches:

- Roll errors, the approach used in [Scagliola et al., 2018] is applied in case the satellite is rolled of about 0.4 deg. It is proposed here to verify if the roll can be calibrated exploiting operational interferometric acquisitions without rolling the satellite. The procedure and the results of the analysis are described in Section 3.1
- Pitch errors, the approach used in [Scagliola et al., 2015] is applied to CryoSat-2 and Sentinel-3 stack data in order to assess the potential pitch bias affecting the acquisitions under study. The procedure and the results of the analysis are described in Section 3.2

3.1 Roll angle bias estimation

Exploiting the interferometric capability of CryoSat-2, the interferometric phase related to the first arrival of the echo is used to retrieve the angle of arrival of the scattering in the across-track direction. When SIRAL is commanded in SARin mode, the interferometric phase difference between the echoes from the two antennas is used to retrieve the angle of arrival of the first scattering point in the across-track direction. In fact, the across-track echo direction can be derived by exploiting simple geometry and the precise knowledge of the baseline vector (i.e. the vector between the two antennas centres of phase), that depends on the actual antenna mispointing angles. CryoSat-2 interferometric acquisitions over

ocean can be exploited to retrieve the across-track slope of the ocean surface [Scagliola et al., 2018]. In the Figure 15, the acquisition geometry is sketched.

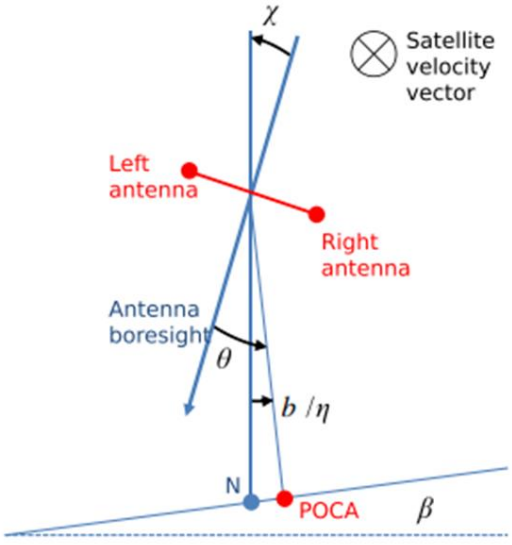

Figure 15. Acquisition geometry in the across-track plane

The interferometer baseline is defined as the versor identifying the direction from the transmitting/receiving antenna phase centre (the left antenna) to the receiving only antenna phase centre (the right antenna). It is kept in flight orthogonal to the ground track so that the roll angle describes the orientation of the interferometer baseline in the across-track plane. We denote the across-track slope of the ocean surface as and the angle made by the direction of first arrival (i.e. Point of Closest Approach, POCA) with antennas' boresight direction as β. Then, the following relation holds

$$\beta = \eta(\theta - \chi) \qquad \text{Eq. 6.}$$

where η is a geometric factor that is given by $\eta = 1 + h/R$ being h the altitude of the satellite with respect the ellipsoid and R is the Earth's radius.

By a priori knowledge of the ocean slope β_{known}, as an example from geoid, it is possible to

1. assess the end-to-end error on the measured angle of arrival by comparison of the measured slope with β_{known}

$$\epsilon_{e2e} = \theta_m - \chi - \frac{\beta_{known}}{\eta} = a\theta + \epsilon_\theta + \epsilon_\chi + \epsilon_\beta \quad \text{Eq. 7.}$$

that includes the following error contributions: phase departure $a\theta$, error contribution from the measured angle of arrival ϵ_θ, error contribution from the baselined orientation ϵ_χ and error contribution from the a priori known slope model of the ocean surface ϵ_β. In particular, as described in the following figure, two different approaches have been compared. As first, the approach currently used for the Cryosat interferometer calibration performed during roll campaigns (where the satellite roll is commanded to values of ±0.4 degrees) has been applied to nominal acquisitions with roll close to 0 degrees, as described in Figure 16 (a). A simple threshold retracker is used to identify the range samples corresponding to the POCA. The angle of arrival is computed as:

$$\theta_m = \frac{\phi(0)}{k_0 B} \quad \text{Eq. 3}$$

where ϕ is the phase difference waveform, evaluated in correspondence of delay equal to 0, i.e. in the POCA. Conversely, a new method has been implemented (see Figure 16 (b)) that makes use of Aresys in-house physical retracker to obtain from the SSH a more reliable estimate of the range samples corresponding to the POCA. Additionally, the SWH is exploited in order to obtain an estimation of the phase departure term, according to the following model:

$$\varphi_d(\theta, \sigma_s) = \mathrm{a}(\sigma_s)\theta = [a_0(1 + b\sigma_s^2 + d\sigma_s^4)]\theta \quad \text{Eq. 4}$$

Where the coefficients are $a_0 = -0.0305$, $b = 0.384m^{-2}$ and $d = -0.024m^{-4}$.

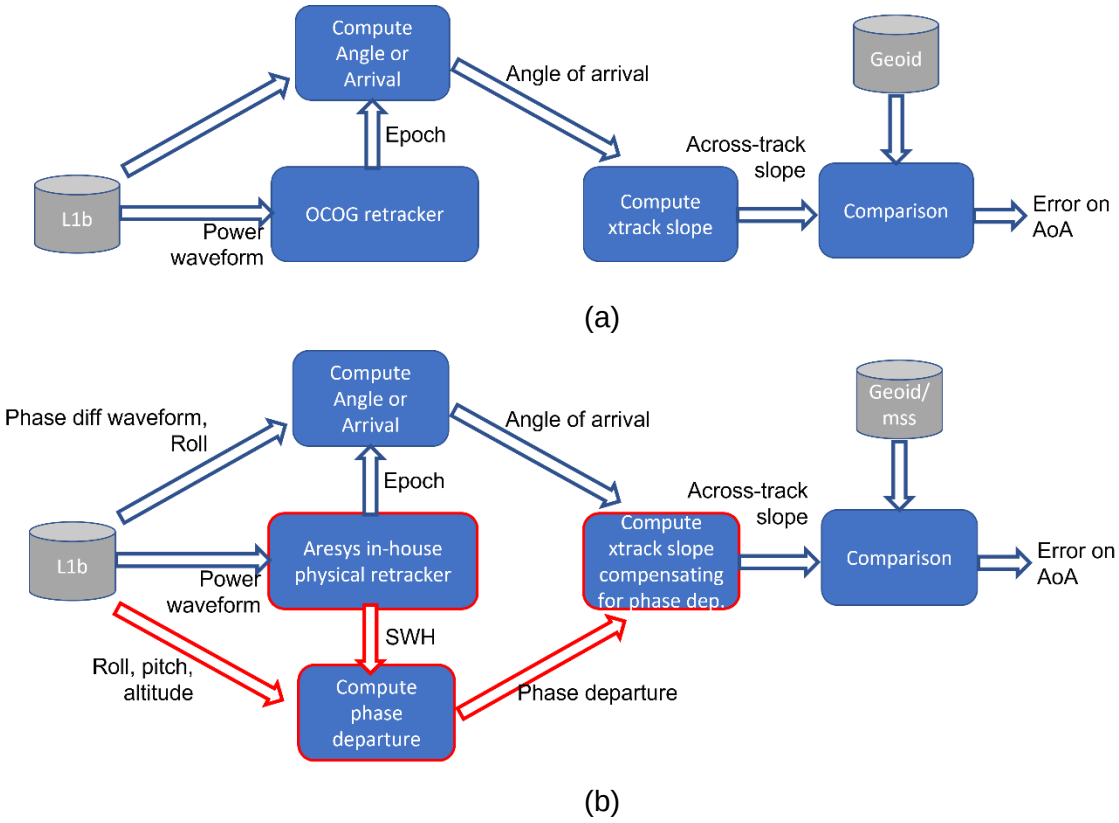

Figure 16. Different approaches for the computation of the AoA error.

2. Compute a calibration function (e.g. linear model)

$$F(\theta) = a\theta + \chi_0 \qquad \text{Eq. 8.}$$

where the linear term a provides an estimate of the phase departure, while the constant term χ_0 provides an estimate of the bias affecting the roll.

3.1.1 Cryosat-2 roll campaigns data analysis

The results obtained by testing the different configurations in case of Cryosat-2 roll campaign data are presented in this section. The roll campaigns from 3 to 11 have been included in this analysis, with acquisition dates ranging from October 2011 to August 2020. The following table provides a list of the analysed datasets.

Roll camp.	Dates	L1b Baseline	STR in use on board	Attitude (roll)		
				STR1	STR2	STR3
Roll3	Oct. 2011	D	3	X		X
Roll4	Sept. 2012	D	3		X	X
Roll5	Oct. 2013	D	2	X	X	
Roll6	Jan. 2014	D	2&3	X	X	X
Roll7	May 2015	D	2	X	X	X
Roll8	Aug. 2016	D	3	X	X	X
Roll9	Feb. 2018	D	1	X	X	X
Roll10	Apr. 2019	D	2	X	X	X
Roll11	Aug. 2020	D	2	X	X	X

The following set of configurations have been used, in order to assess the differences in achievable accuracy and precision.

ID	Retracker	Phase departure correction	Calibration function estimation
ret = EMP, pd = off, cal lin	Empirical	not applied	linear
ret = PHY, pd = off, cal lin	Physical	not applied	linear

ret = PHY, pd = on, cal lin	Physical	applied	linear
ret = PHY, pd = on, cal bias	Physical	applied	constant

The following figure presents the comparison between the estimated calibration function terms for the analysed configurations.

Figure 17 (a) provides a comparison of the phase departure term estimated from the end-to-end error measured on the angle of arrival. As expected the “cal bias” case present a constant term equal to 0, since a constant calibration function is assumed in this case. Moreover, as expected, the estimated term a is almost equal to zero also when the phase departure correction has been applied to data before the calibration function correction (“pd on” case).

Figure 17 (b) provides a comparison of the roll bias estimated from the end-to-end error measured on the angle of arrival. The estimated bias is quite consistent for all analysed cases, with an average value of -0.002 rad and a slightly increasing trend of -9.4 microrad/year. It is worth noticing that, for these analyses, the compensation of the known roll has been performed starting from reprocessed Star Tracked attitude information instead of using the attitude annotated in the L1B input files.

The results on the across track accuracy estimation are shown in Section 4.1.1.

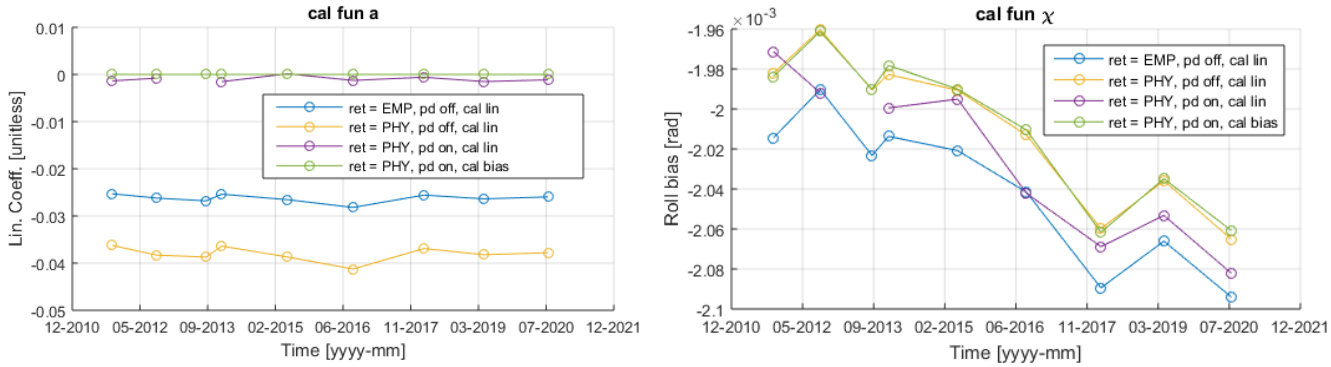

(a) (b)

Figure 17. Calibration function evaluation for Cryosat-2 roll campaigns data: linear term (a) and roll bias (b).

3.1.2 Cryosat-2 nominal acquisitions data analysis

A set of Cryosat-2 L1B data over Greece has been selected as test dataset. A total of 123 data were selected, with acquisition dates ranging from June 2018 to December 2018.
For each of the available L1B, the related L2 generated from Aresys sepcialized SARIn retracker has been considered, in order to compare the performances of the two methods presented in Figure 16 (a) and (b).

The following set of configurations have been used, in order to assess the differences in achievable rool bias estimation.

ID	Retracker	Phase departure correction	Calibration function estimation
ret = EMP, pd = off, cal lin	Empirical	not applied	linear
ret = EMP, pd = on, cal lin	Empirical	applied	linear
ret = EMP, pd = on, cal bias	Empirical	applied	constant
ret = PHY, pd = off, cal lin	Physical	not applied	linear
ret = PHY, pd = on, cal lin	Physical	applied	linear
ret = PHY, pd = on, cal bias	Physical	applied	constant

With respect to the roll campaigns, two additional configurations have been considered, i.e.:

- the possibility to compensate for the phase departure term when using an empirical retracker (“ret = EMP, pd = on, cal lin”). In this case the phase departure model is initialized assuming a constant SWH value of 2m;

- the possibility to compensate for the phase departure term when using an empirical retracker (“ret = EMP, pd = on, cal bias”) but using a constant calibration function. In this case the phase departure model is initialized assuming a constant SWH value of 2m;

These two additional configurations have been considered because, in the analysed coastal zone, the reliability of the physical retracker might be impaired form the presence of land contamination in the L1B waveforms.

The following figure presents the comparison between the estimated calibration function terms for the analysed configurations.

Figure (a) provides a comparison of the phase departure term estimated from the end-to-end error measured on the angle of arrival. As expected the “cal bias” case present a constant term equal to 0, since a constant calibration function is assumed in this case. Moreover, differently from the roll campaigns case, the estimated term a is not very close to zero when the phase departure correction has been applied to data before the calibration function correction (“pd on” case). This might be explained by an inaccurate estimation of the SWH input values used for the phase departure model initialization. However, it can be noticed that, as expected, when using the SWH estimated from Aresys physical retracker (“ret = PHY, pd = on, cal lin”) the estimated value of a is sensibly smaller than the case where a constant value of SWH 0 2m is assumed (“ret = EMP, pd = on, cal lin”).

Figure (b) provides a comparison of the roll bias estimated from the end-to-end error measured on the angle of arrival. As expected, the estimated bias is quite consistent in case the phase departure is compensated or not, but shows a dependence on the type of retracker used, with an average difference of 20.75 microrad in case a linear calibration function is assumed (“ret = EMP, … , cal lin” vs “ret = PHY, … , cal lin”) and of 40.23 microrad in case a constant calibration function (“ret = EMP, … , cal bias” vs “ret = PHY, … , cal bias”) is used. It is worth noticing that, for these analyses, the compensation of the known roll has been performed starting from the attitude annotated in the L1B input files. This explains the different bias estimated with respect to the roll campaigns case.

The results on the across track accuracy estimation are shown in Section 4.1.2.

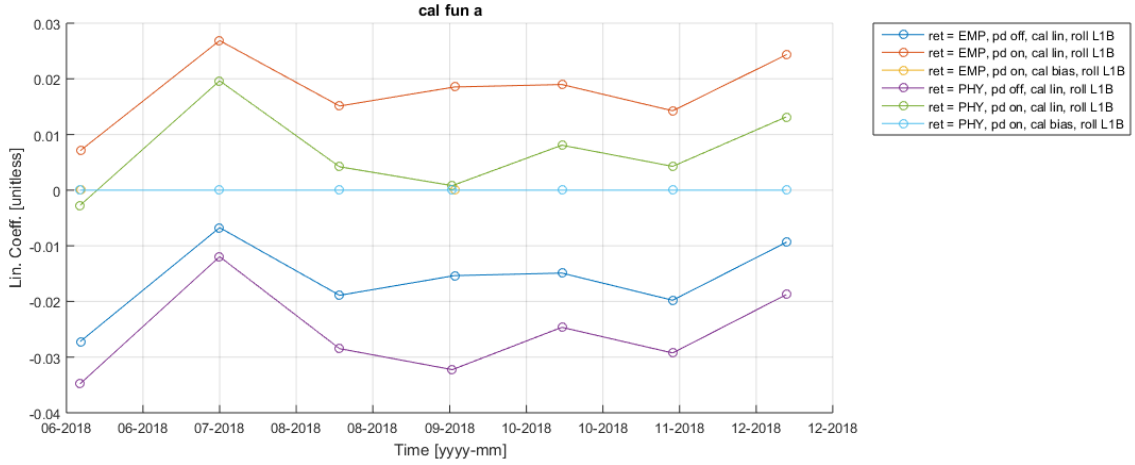

(a)

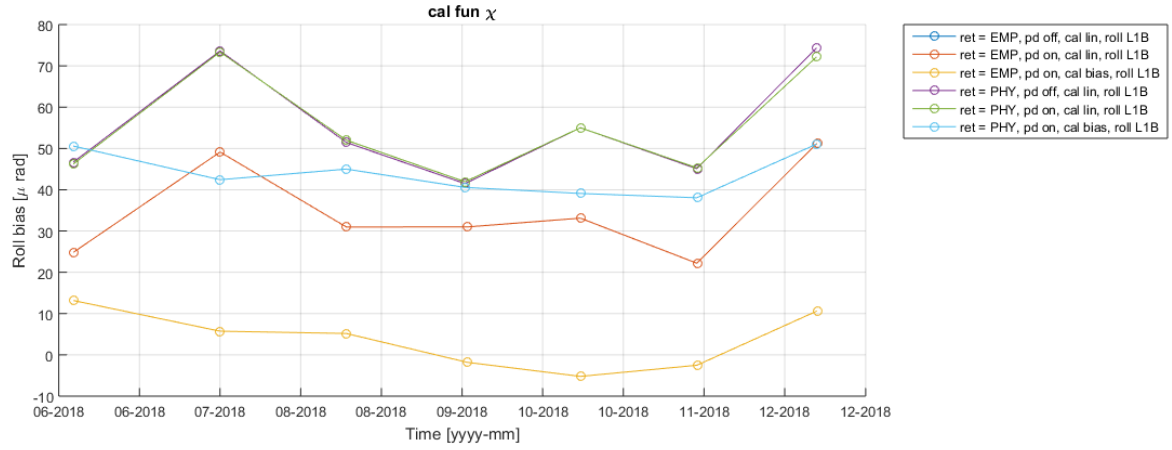

(b)

Figure 18. Calibration function evaluation for Cryosat-2 roll campaigns data: linear term (a) and roll bias (b).

3.2 Pitch angle bias estimation

The analysis is aimed at obtaining an independent estimate of the pitch mispointing angle based only on the L1B-S data stack. This method is based on the analysis of the power modulation of the single look echoes that compose the stack by fitting the along-track antenna pattern in order to determine the actual pitch of the satellite. The input of the analysis are the L1B-S products. This product is an intermediate and optional output of the Delay/Doppler processing that contains for each Surface Sample the collection

of all the Delay/Doppler processed and calibrated complex single look echoes, arranged in stacks after slant range correction and prior to multilooking. The procedure consists in processing each stack of the product, collecting all the single look echoes coming from the processed bursts illuminating the same location on ground (i.e. the surface sample), in order to obtain an estimation of the pitch mispointing. This can be obtained since, in case of a uniformly backscattering rough surface such as open ocean, the power of the single looks in a surface sample stack is mainly modulated by the along track antenna pattern [Scagliola et al., 2015]. For each stack, the processor computes the Range Integrated Power (RIP) of the single look echoes as function of the look angle and performs a least-squares fit of the Gaussian along-track antenna pattern. The maximum of the fitted along-track antenna pattern is located in correspondence of the pitch angle and provides and independent estimation of the pitch angle.

Reading of input L1BS NetCDF file.

Initialization of the internal data structure containing all needed information for the stack analysis and fitting.

A zero mask is applied to the power stack in order to remove the effect of Doppler ambiguities.

Range bin are selected by:
- Averaging of the power stack X(τ, ξ_n) over the N single looks;
- Threshold retracking on the multilooked waveform to identify leading edge start (τ_s) and stop (τ_e) range bins

Removal of single looks:
- with zeros coming from ambiguity masking in correspondence of the leading edge
- providing a neglectable power contribution

The range integrated power is computed as: $RIP(\xi_n) = \sum_{\tau=\tau_s}^{\tau_e} X(\tau, \xi_n)$

The along-track antenna power modulation as a function of the look angle is given by $G_{az}(\xi) = exp\left\{-\frac{(\xi-\eta)^2}{\gamma^2}\right\}$ where η is the pitch angle and γ the along-track antenna aperture. Nonlinear least square fitting is used to estimate the pointing direction η of the along-track antenna pattern with respect to the nadir from $RIP(\xi_n)$.

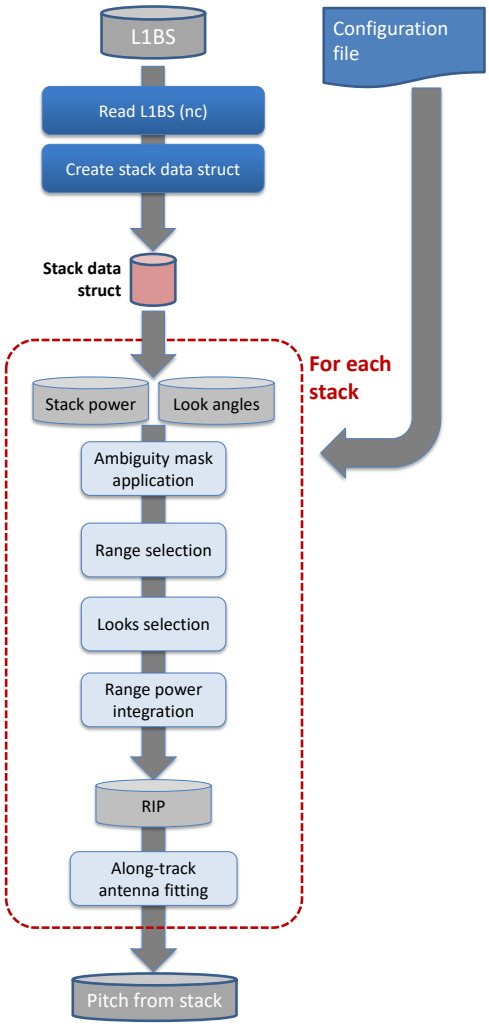

Figure 19. Pitch angle estimation: processing steps.

Recalling that on a uniformly rough spherical surface, e.g., the ocean, the power of the single-look echoes in a surface sample stack is modulated by the along-track antenna pattern, the look angle for a given surface sample is here defined as the angle at which the surface sample itself is seen with respect to the nadir direction.

Recalling that the antenna gain pattern in is approximately separable into its along- and across-track components, the power of the single-look echoes can be written as a function of the delay τ and of the look angle ξ as

$$X(\tau,\xi) = A\ exp\left[-\frac{2(\xi-\mu-\frac{\varsigma}{\eta})}{\gamma_1^2}\right]\mathrm{F}(\tau) \qquad \text{Eq. 9.}$$

where the first term A is a constant, $F(\ \ )$ denotes a function of the delay (including the across-track antenna pattern), and the second term is the power gain given by the along-track antenna pattern as a function of the look angle ξ, the pitch μ, and the along-track component of the surface vector gradient scaled by a geometrical factor ς/η. It has to be remarked here that in the formula above the unknown ς/η is summed with the pitch, as a consequence an accurate knowledge of the surface slope is needed to retrieve the pitch estimates with sufficient accuracy. The proposed method to derive the along-track component of the surface vector ς as the only inputs the stack of single-look echoes and the look angle associated to each echo. Starting from those inputs, the following quantities are sequentially computed:

1. Power of the single-look echo
2. Integration in time delay: The power distribution as a function of the look angle only is computed by integrating the power stack for the time delay corresponding to the leading edge. Since the leading edge of the echo corresponds to the along-track strip at the nadir of the instrument, so aiming at avoiding the dependence on the across-track pattern, it is reasonable in to sum only the power contributions from the leading edge.
3. Along-track antenna pattern fitting: Nonlinear least square fitting is used to estimate the location of the maximum of the antenna pattern.

The proposed method returns values at 20 Hz frequency, i.e., one for each surface sample; anyway, those measurements are expected to be affected by noise. The values retrieved at 20 Hz can be averaged at 01Hz to increase the accuracy of the estimate.

Following the estimation of the 20Hz values of the pitch from the L1BS data, the procedure described in the following figure is applied in order to obtain an estimation of the bias affecting the pitch values.

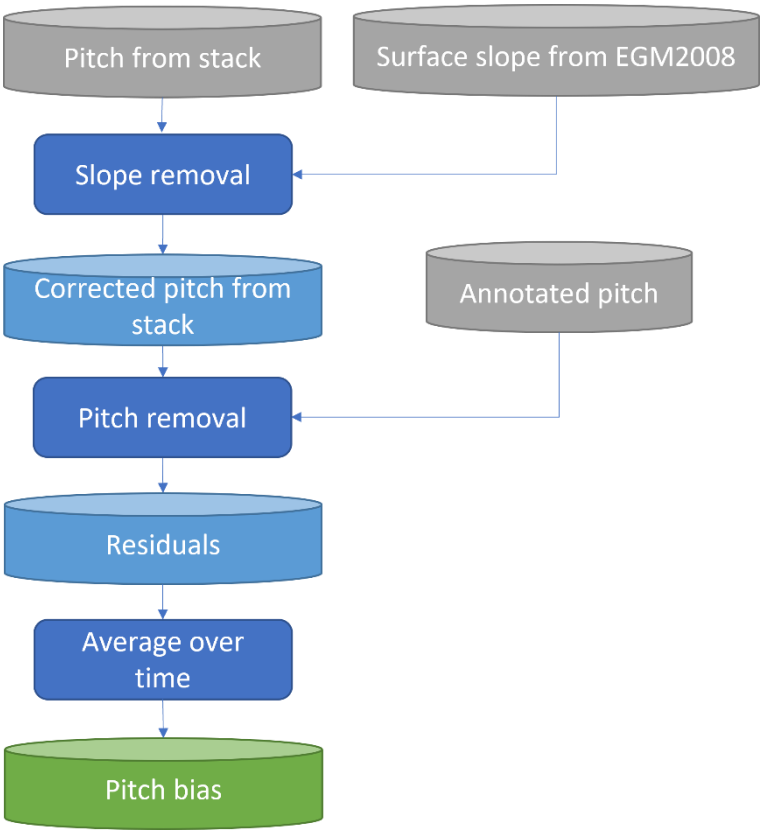

Figure 20. Pitch bias estimation: processing steps.

The measurements obtained from the L1BS stack, i.e. the look angle associated to the maximum of the antenna pattern fitted to the RIP, consists in the sum of the contributions of:

- The pitch angle of the satellite;
- The along track slope of the surface;

The first step of the procedure consists in the removal of the slope contribution (evaluated during the processing starting from the EGM2008 model in correspondence of the ground track locations of the input datasets) from the estimated measurements. According to Cryosat-2 convention, being a positive pitch representative of a nose down, and according to the sign of the slopes retrieved by the processor (positive slopes associated to up-hill slopes in the flight direction), the estimated slope is removed from the pitch from stack measurements.

The second step of the procedure is the removal of the pitch annotated in the input data. By averaging over time the residuals obtained form this step the bias affecting the pitch measurements can be estimated. Please note that this procedure can be applied both to 20Hx and 01Hz averaged values. In the following sections, the results obtained form the analysis of the Sentinel-3A, Sentinel-3B and Cryosat-2 datasets over Greece are presented.

3.2.1 Sentinel-3A data analysis

Sentinel-3 L1B Stack data available over Greece has been selected as test dataset. A total of 352 data were available, with acquisition dates ranging from June 2018 to November 2019.

Figure 21 (a) provides the time series of the 20-Hz pitch measurements obtained by the stack processing after the removal of the slope contribution. As can be observed, the estimation converges to two distinct set of values, as two different series over time can be easily noticed:

- One time series is centred around the 0 and presents values similar to the pitch annotated in the products.
- The second time series is centred around -0.15 degrees, thus showing a large bias with respect the pitch values annotated in the products.

Upon further inspection it has been verified that the two different time series refer respectively to Descending (centred around 0 degrees) and Ascending (centred around -0.15 degrees) passes of the satellite. The two set of data has been consequently analysed separately.

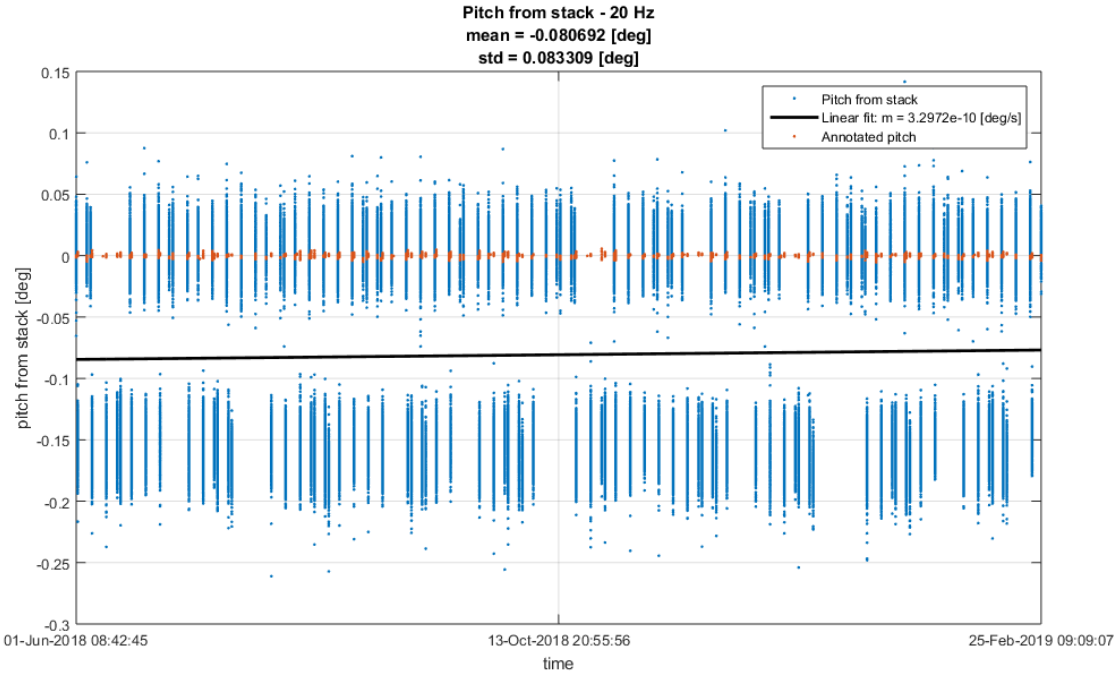

(a)

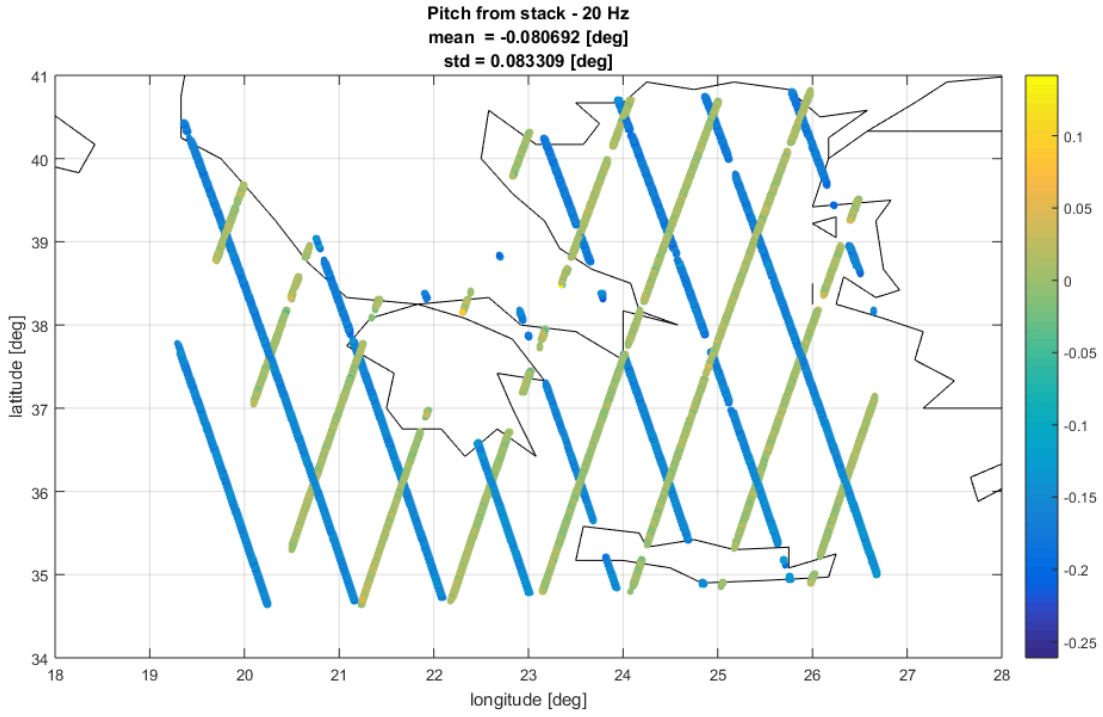

(b)

Figure 21. Pitch from stack estimated from Sentinel-3A data: (a) 20Hz time series and (b) geographical location.

3.2.1.1 Ascending passes

The results obtained from the analysis of the available Sentinel-3A ascending passes are described in this section.

Figure 22 (a) provides the time series of the 20-Hz pitch measurements obtained by the stack processing after the removal of the slope contribution, while Figure 22 (b) provides the same values as function of the geographical locations.

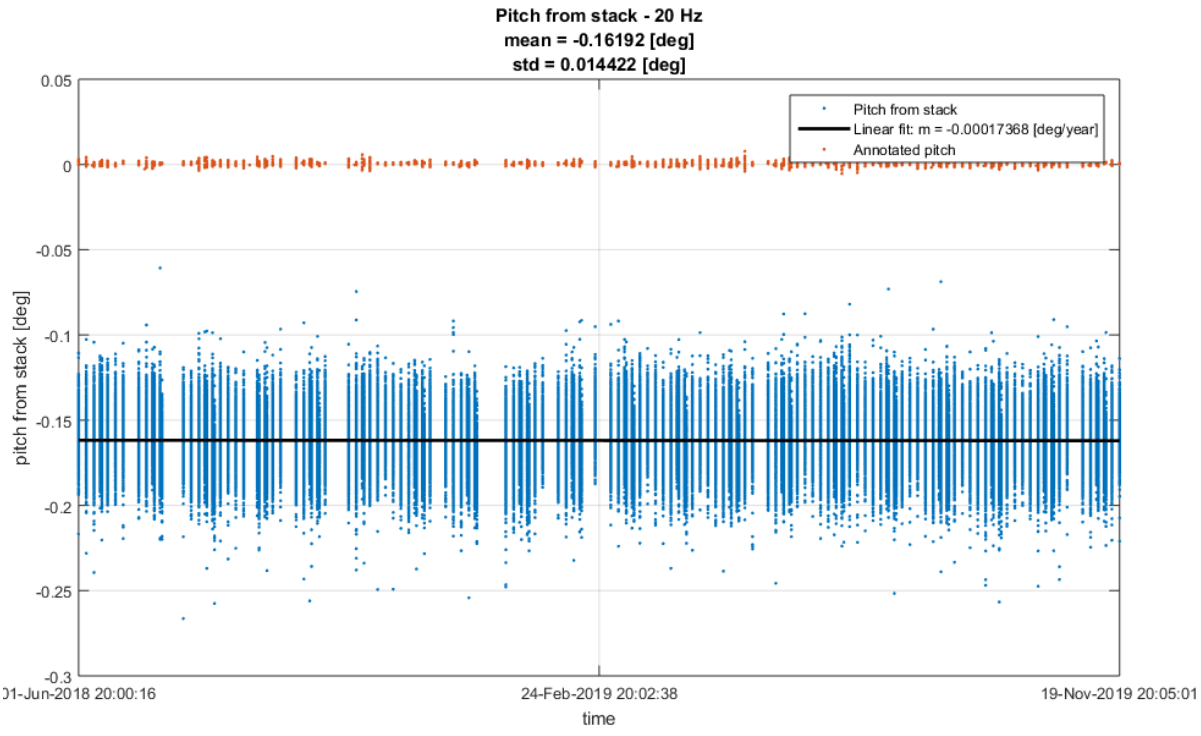

(a)

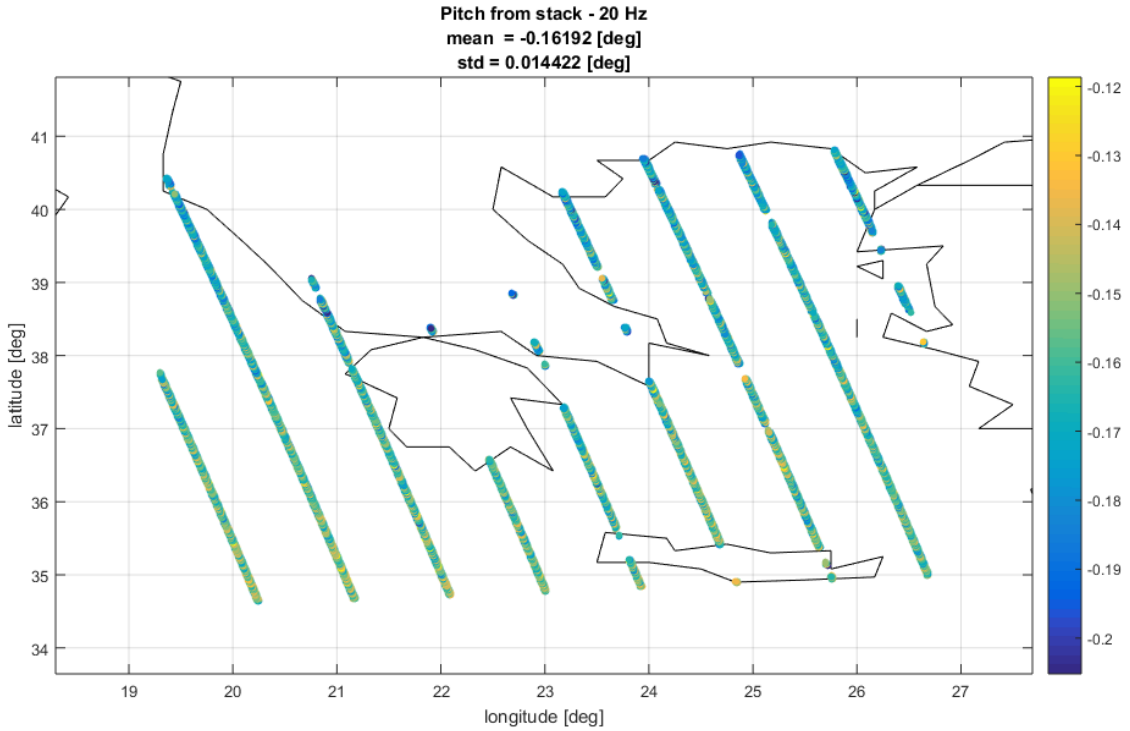

(b)

Figure 22. Pitch from stack estimated from Sentinel-3A ascending passes: (a) 20Hz time series and (b) geographical location.

An average pitch bias of -0.161 degrees has been measured from Sentinel-3A descending passes. The bias seems quite stable in time, with a negligible estimated linear trend of 2.9738e-05 deg/year. The residual variability of the measured bias can be addressed to an incorrect retrieval of the surface slope from the geoid model and to local variations of the dynamically evolving ocean surface. An estimation of the error on the surface slope measurement is provided in Section 4.2.2.

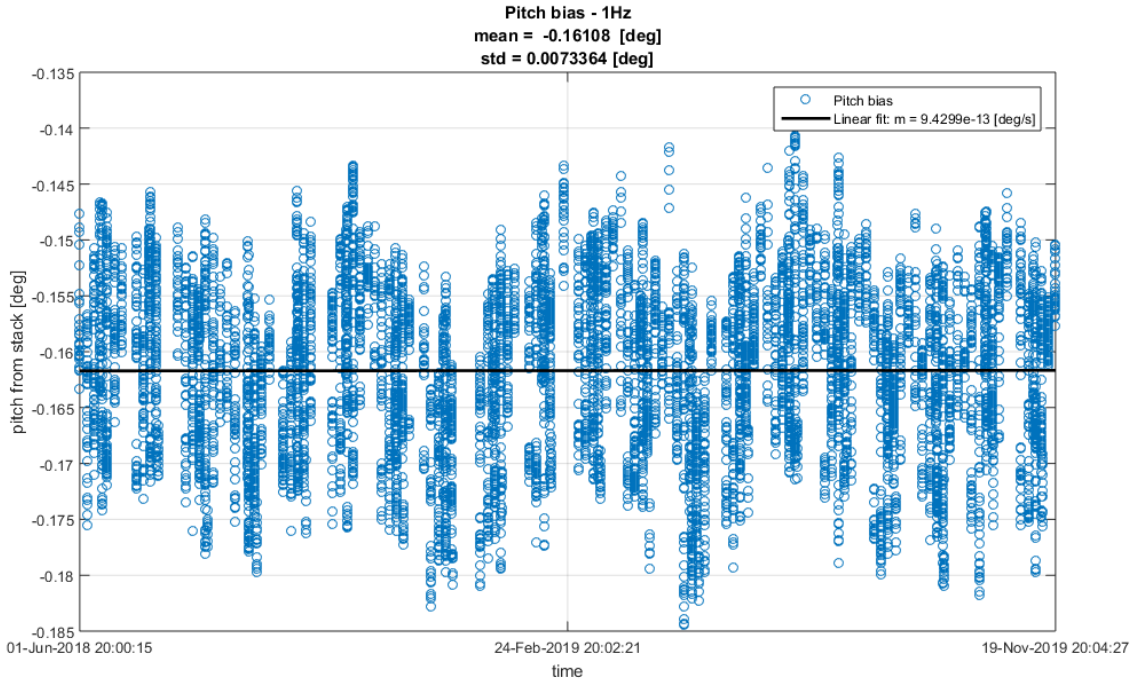

(a)

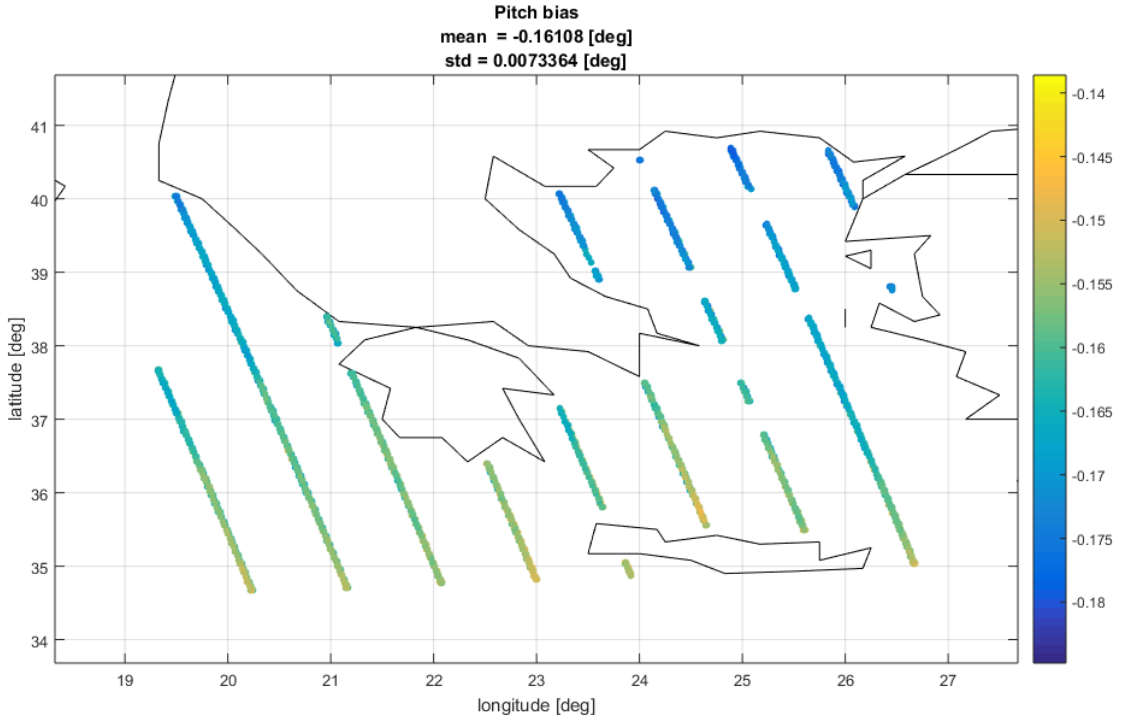

(b)

Figure 23. Pitch bias estimated from Sentinel-3A ascending passes: (a) 01Hz time series and (b) geographical location.

Additional tests have been performed in order to understand the reason for this large pitch bias. The following Figure provides a comparison of the stack as function of the look angle and the range bin (top) and the associated RIP power as a function of the look angle read from two different L1BS files from ascending (a) and descending (b) passes. From the analysis of the stack and of the RIP it is evident that the look angles annotated are quite different in case of ascending and descending passes, thus explaining the different estimates retrieved form the processor. The reason of this difference in the annotated data should be further investigated, and the pitch bias estimated from this dataset reassessed.

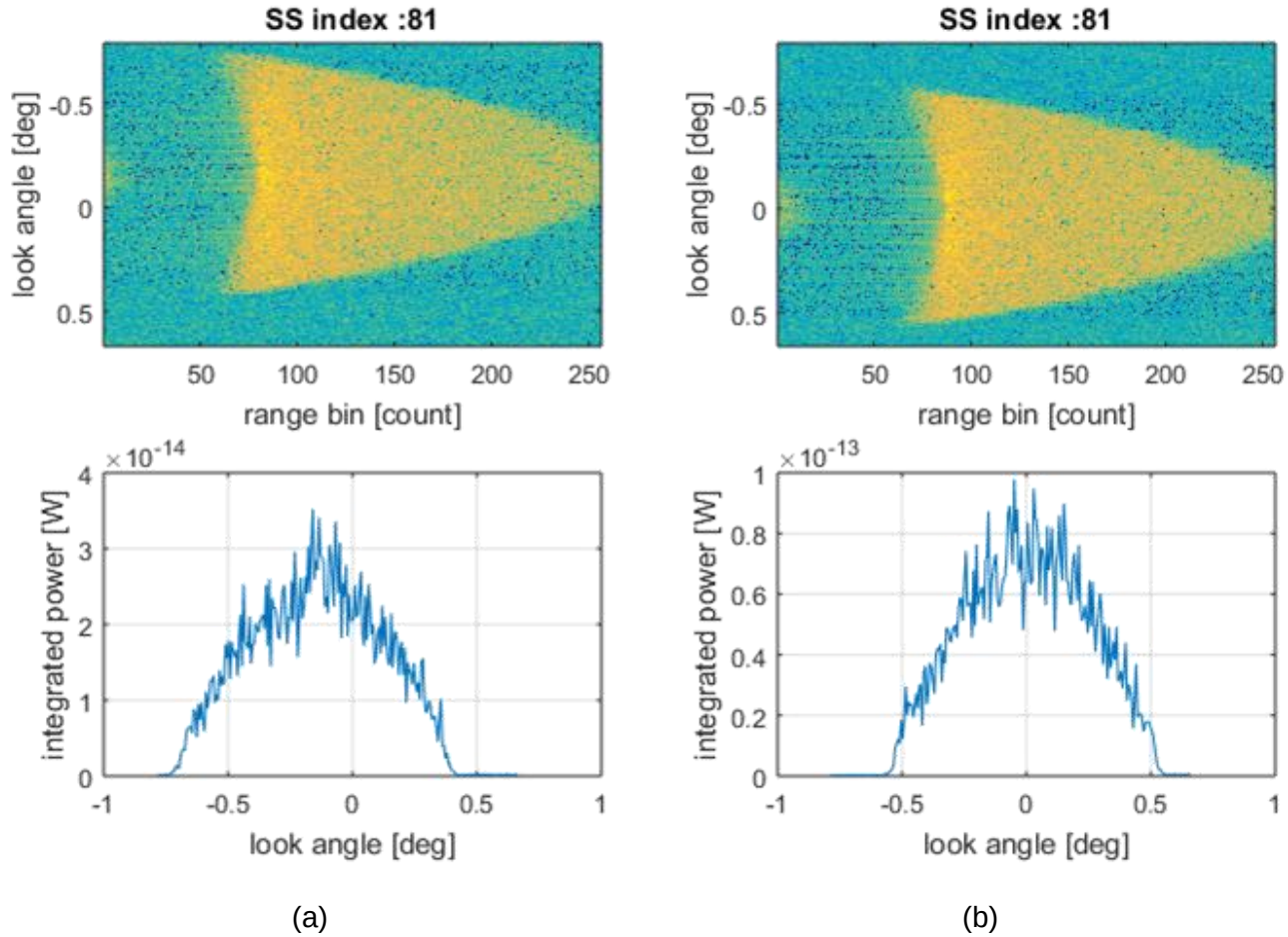

(a) (b)

Figure 24. Stack power and associated RIP for one Surface Sample in the L1B data: (a) ascending and (b) descending pass.

3.2.1.2 Descending passes

The results obtained from the analysis of the available Sentinel-3A descending passes are described in this section. Figure 25 (a) provides the time series of the 20-Hz pitch measurements obtained by the stack processing after the removal of the slope contribution, while Figure 25 (b) provides the same values as function of the geographical locations.

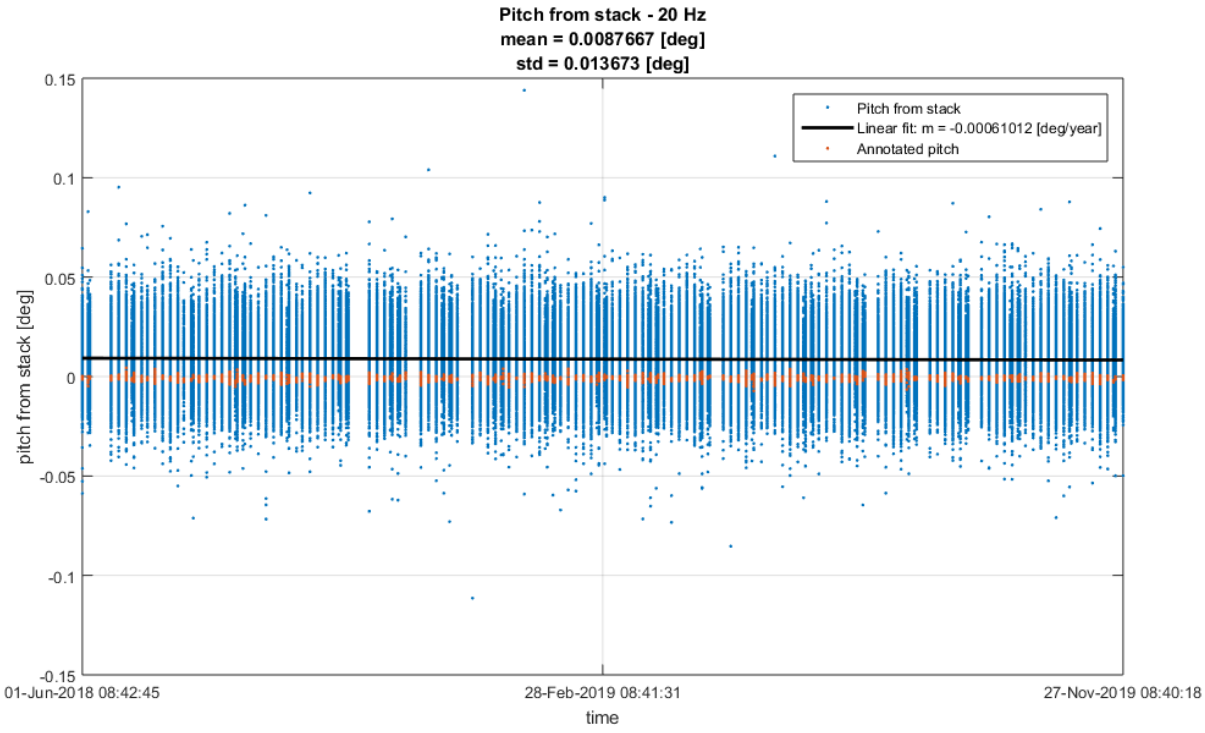

(a)

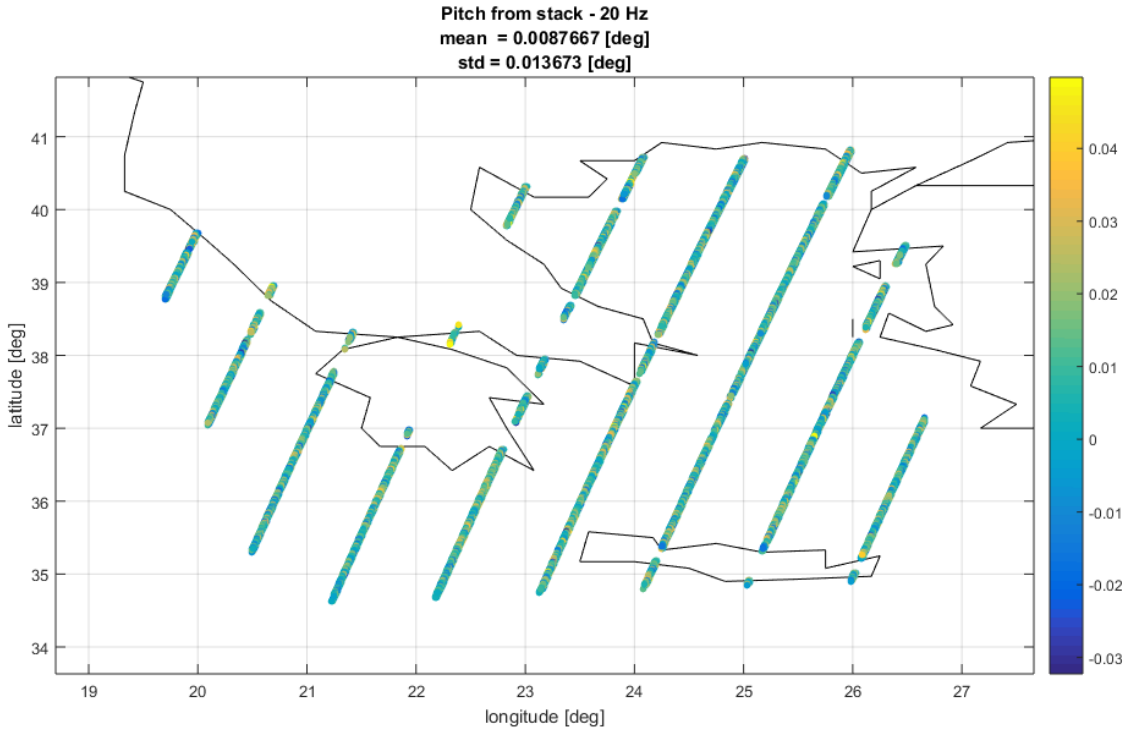

(b)

Figure 25. Pitch from stack estimated from Sentinel-3A descending passes: (a) 20Hz time series and (b) geographical location.

An average pitch bias of 0.0088 degrees has been measured from Sentinel-3A descending passes. The bias seems quite stable in time, with a negligible estimated linear trend of -3.0483e-04 deg/year. The residual variability of the measured bias can be addressed to an incorrect retrieval of the surface slope from the geoid model and to local variations of the dynamically evolving ocean surface. An estimation of the error on the surface slope measurement is provided in Section 4.2.1.

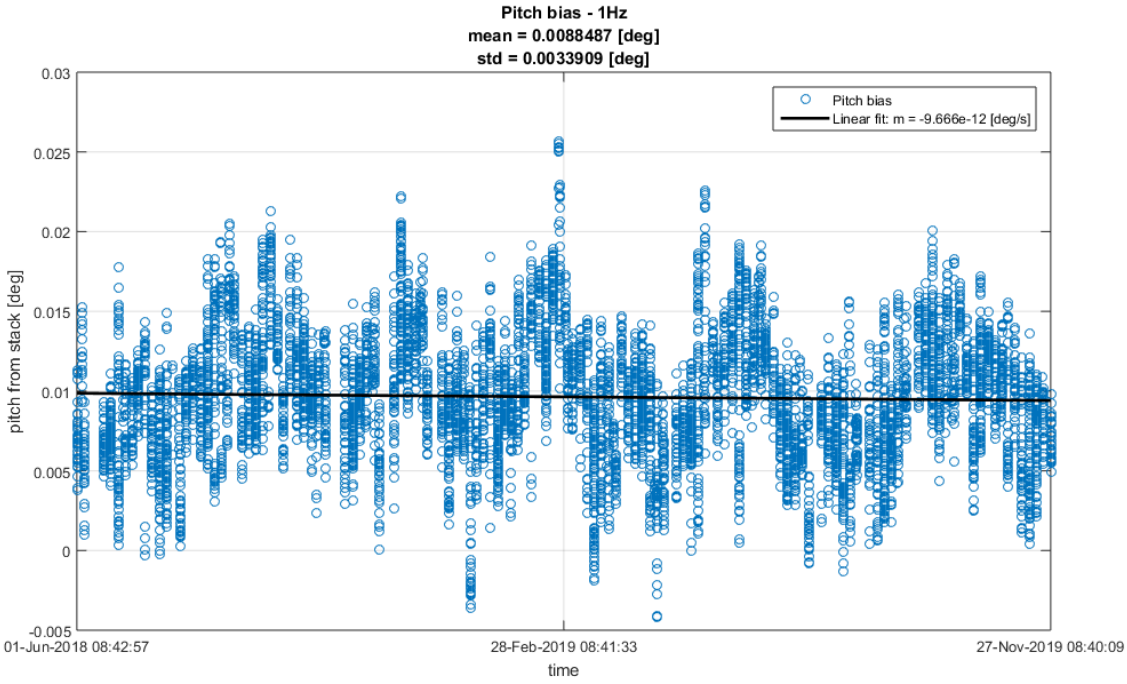

(a)

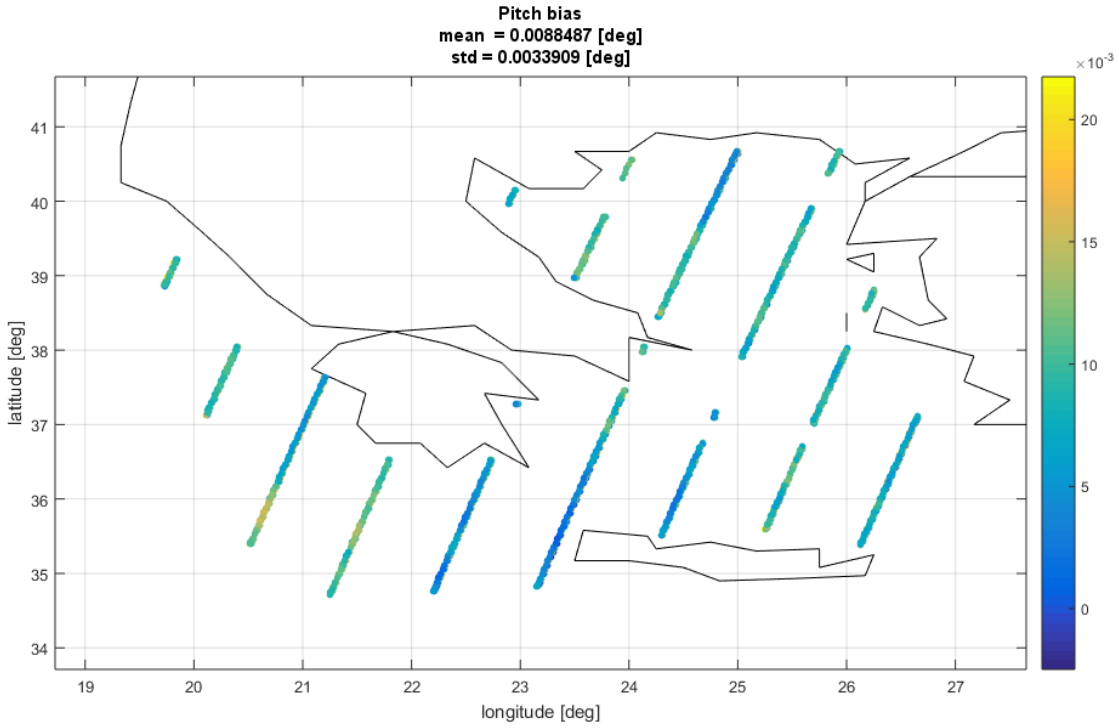

(b)

Figure 26. Pitch bias estimated from Sentinel-3A descending passes: (a) 01Hz time series and (b) geographical location.

3.2.2 Sentinel-3B data analysis

Sentinel-3 L1B Stack data available over Greece has been selected as test dataset. A total of 270 data were available, with acquisition dates ranging from November 2018 to November 2019.
Figure 27 (a) provides the time series of the 20-Hz pitch measurements obtained by the stack processing. As can be observed, the estimation converges to two distinct set of values, as two different series over time can be easily noticed:

- One time series is centred around the 0 and presents values similar to the pitch annotated in the products.
- The second time series is centred around -0.15 degrees, thus showing a large bias with respect the pitch values annotated in the products.

Upon further inspection it has been verified that the two different time series refer respectively to Descending (centred around 0 degrees) and Ascending (centred around -0.15 degrees) passes of the satellite. The two set of data has been consequently analysed separately.

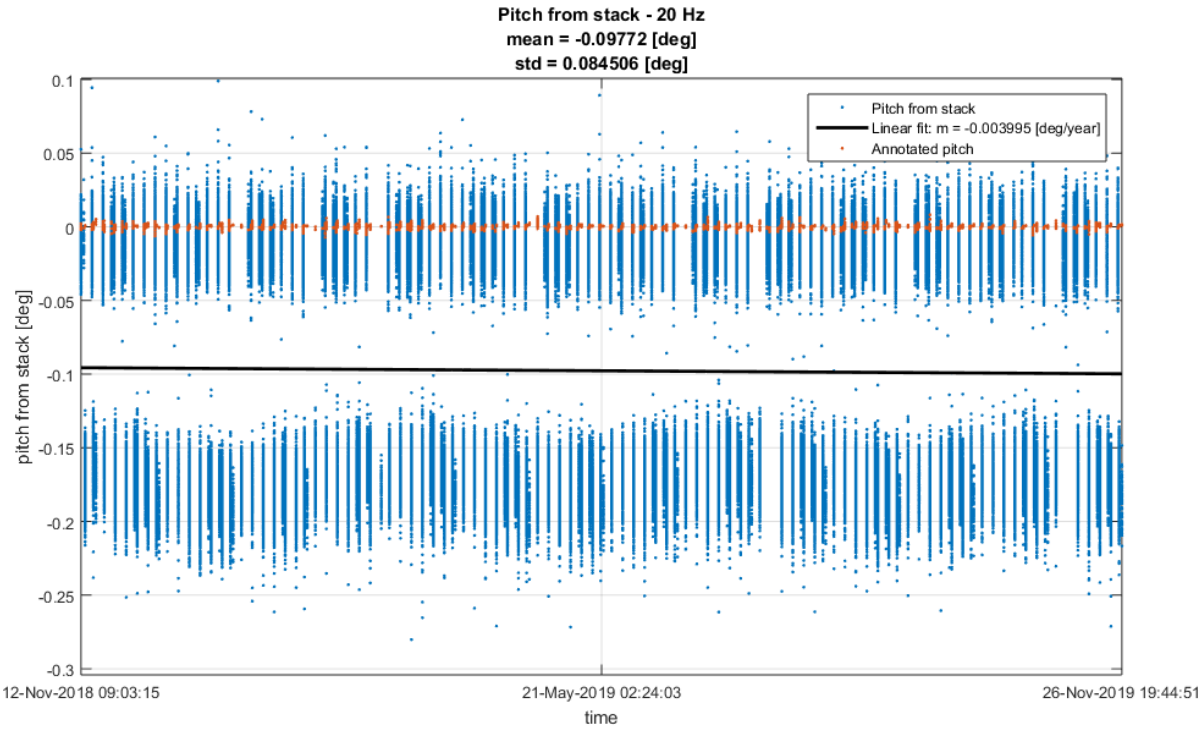

(a)

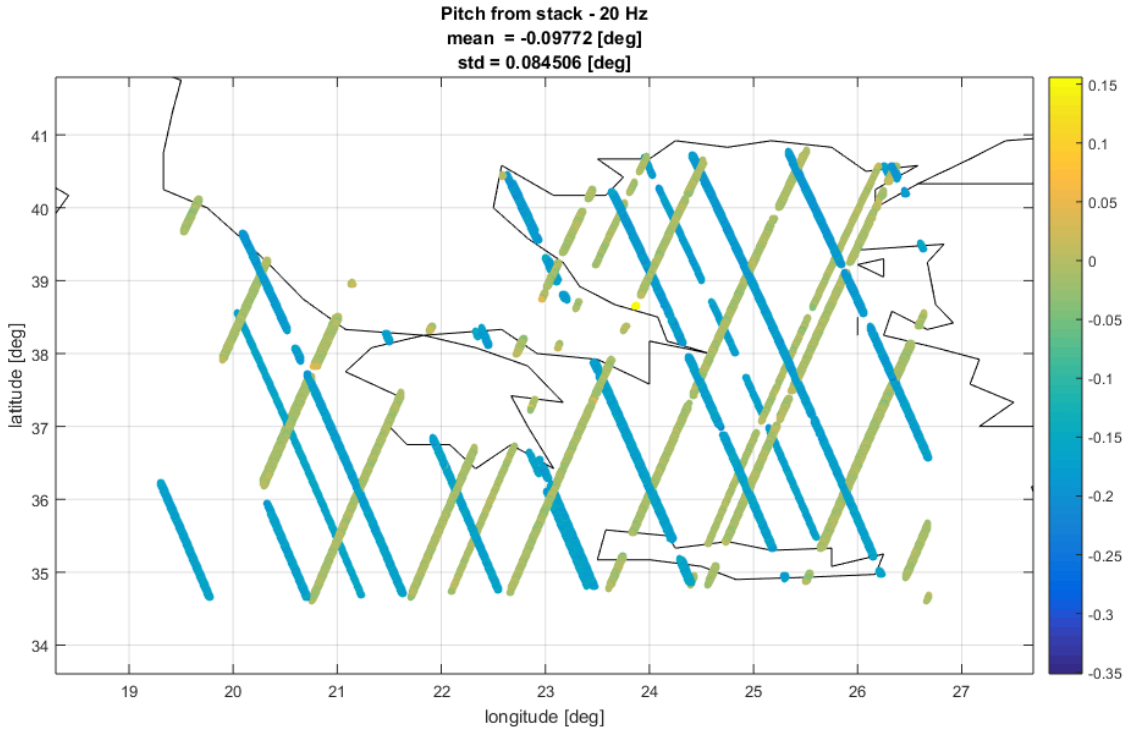

(b)

Figure 27. Pitch from stack estimated from Sentinel-3B data: (a) time series and (b) geographical location.

3.2.2.1 Ascending passes

The results obtained from the analysis of the available Sentinel-3B ascending passes are described in this section. Figure 28 (a) provides the time series of the 20-Hz pitch measurements obtained by the stack processing after the removal of the slope contribution, while Figure 28 (b) provides the same values as function of the geographical locations.

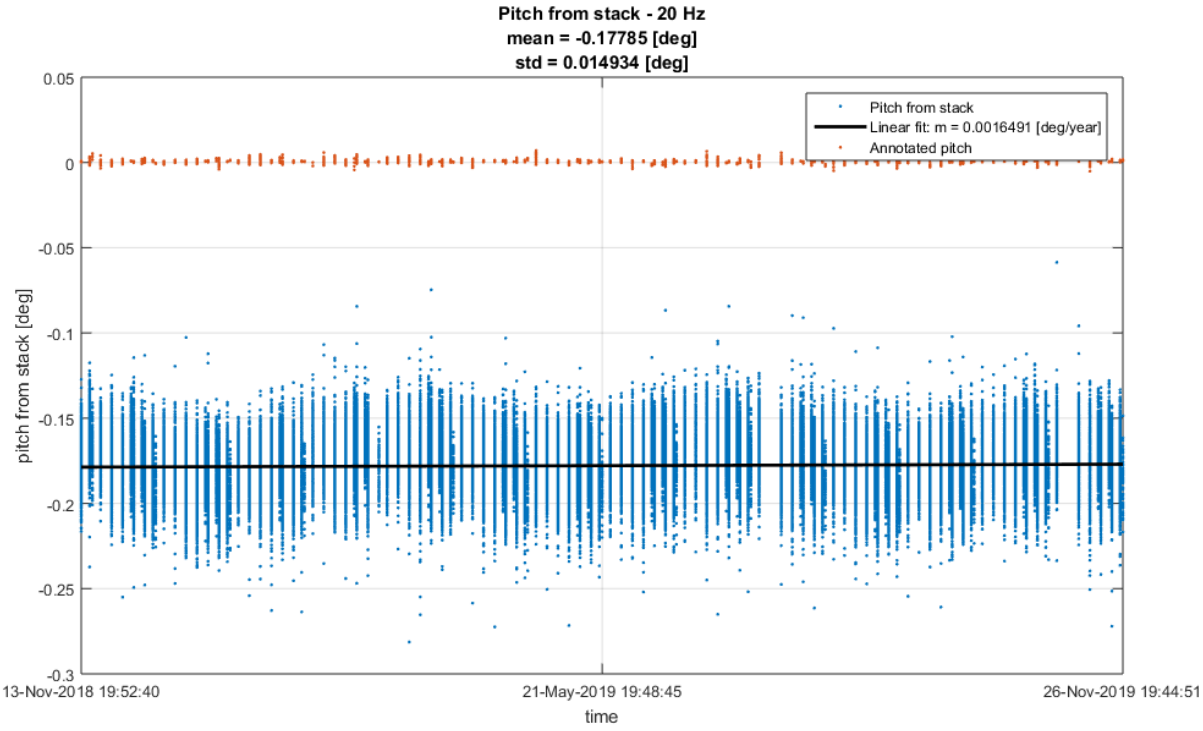
Pitch from stack - 20 Hz
mean = -0.17785 [deg]
std = 0.014934 [deg]
Pitch from stack
Linear fit: m = 0.0016491 [deg/year]
Annotated pitch
pitch from stack [deg]
0.05
0
-0.05
-0.1
-0.15
-0.2
-0.25
-0.3
13-Nov-2018 19:52:40
21-May-2019 19:48:45
26-Nov-2019 19:44:51
time

(a)

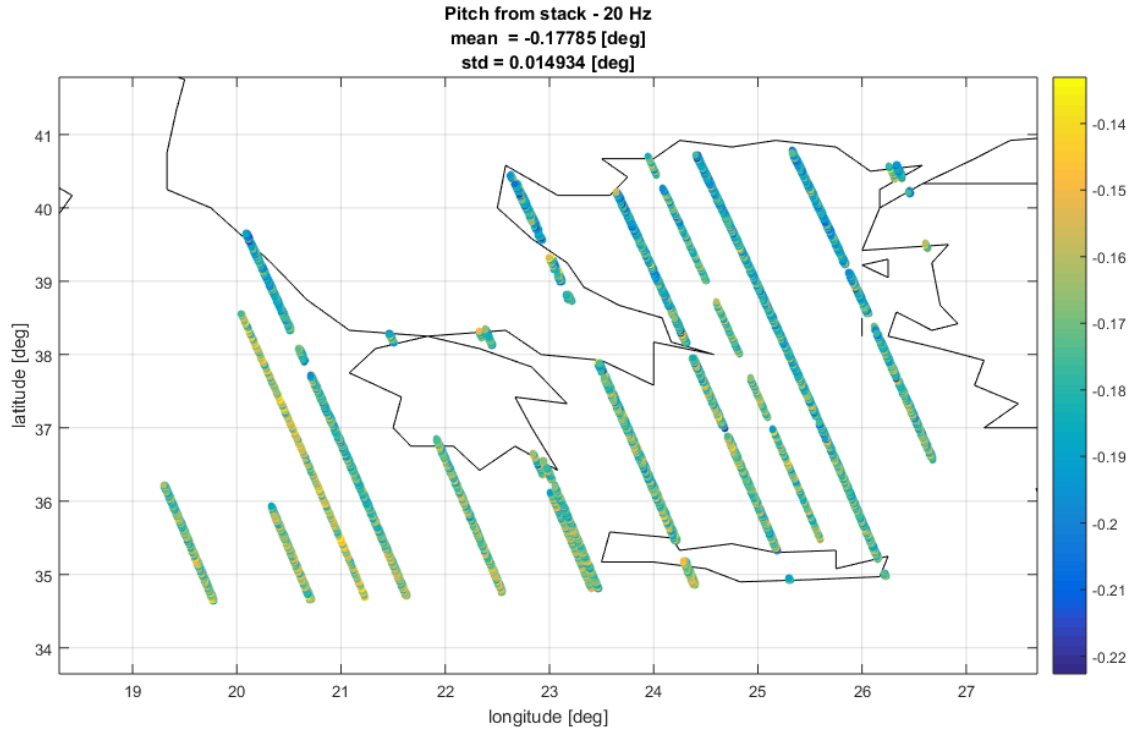
Pitch from stack - 20 Hz
mean = -0.17785 [deg]
std = 0.014934 [deg]
latitude [deg]
41
40
39
38
37
36
35
34
19
20
21
22
23
24
25
26
27
longitude [deg]
-0.14
-0.15
-0.16
-0.17
-0.18
-0.19
-0.2
-0.21
-0.22

(b)

Figure 28. Pitch from stack estimated from Sentinel-3B ascending passes: (a) 20Hz time series and (b) geographical location.

An average pitch bias of -0.1777 degrees has been measured from Sentinel-3B descending passes. The bias seems quite stable in time, with a small estimated linear trend of 0.0026 deg/year. The residual variability of the measured bias can be addressed to an incorrect retrieval of the surface slope from the geoid model and to local variations of the dynamically evolving ocean surface. An estimation of the error on the surface slope measurement is provided in Section 4.2.2.

Additional tests have been performed in order to understand the reason for this large pitch bias with results similar to those shown in Section 3.2.1.1. From the analysis of the stack and of the RIP it is evident that the look angles annotated are quite different in case of ascending and descending passes, thus explaining the different estimates retrieved form the processor. The reason of this difference in the annotated data should be further investigated, and the pitch bias estimated from this dataset reassessed.

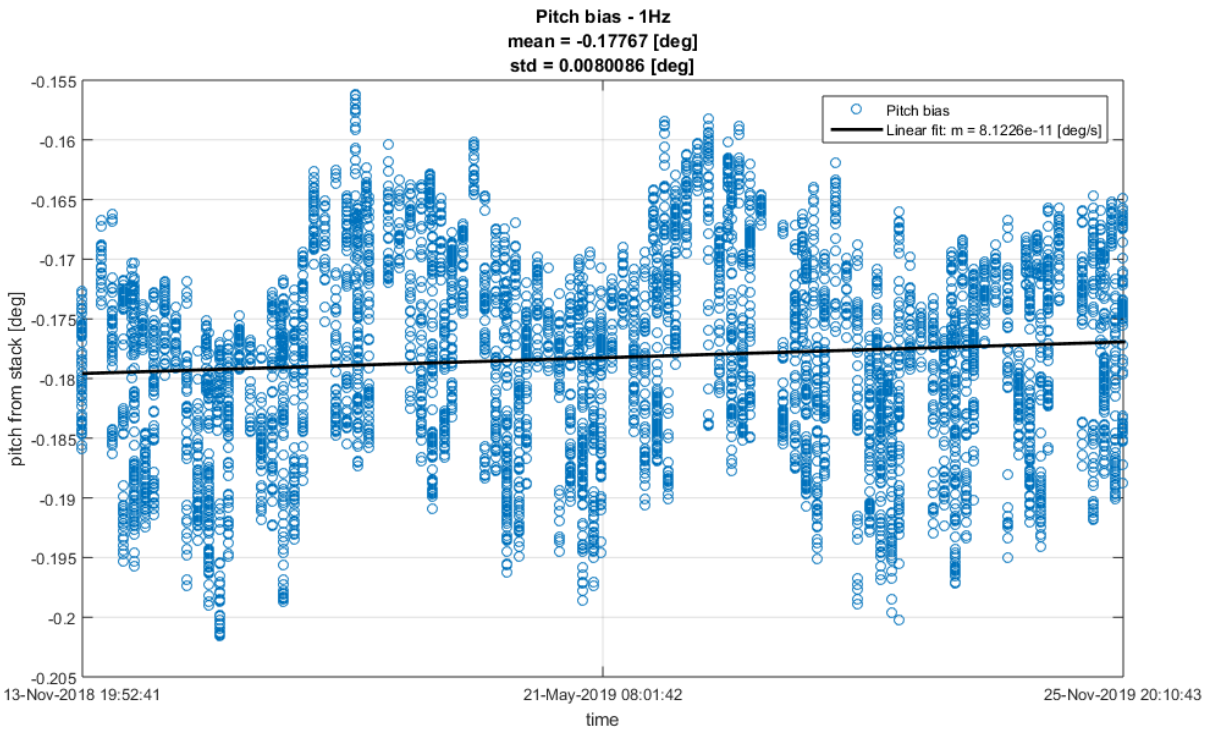

(a)

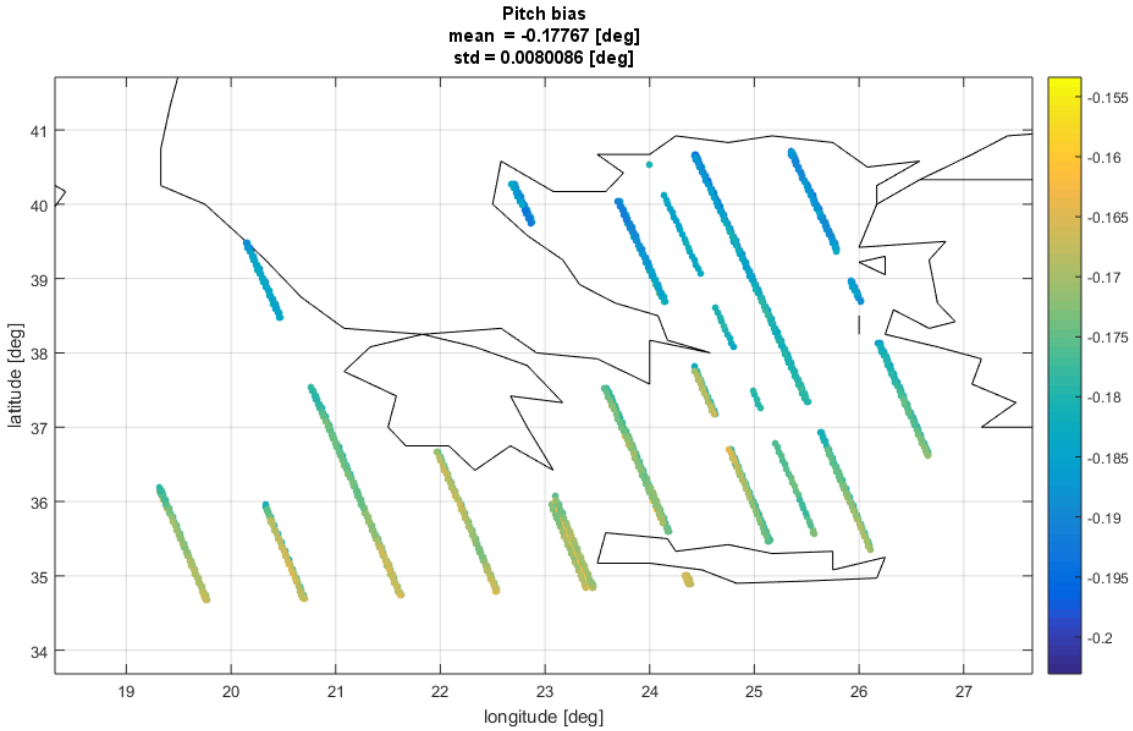

(b)

Figure 29. Pitch bias estimated from Sentinel-3B ascending passes: (a) 01Hz time series and (b) geographical location.

3.2.2.2 Descending passes

The results obtained from the analysis of the available Sentinel-3B descending passes are described in this section. Figure 30 (a) provides the time series of the 20-Hz pitch measurements obtained by the stack processing after the removal of the slope contribution, while Figure 30 (b) provides the same values as function of the geographical locations.

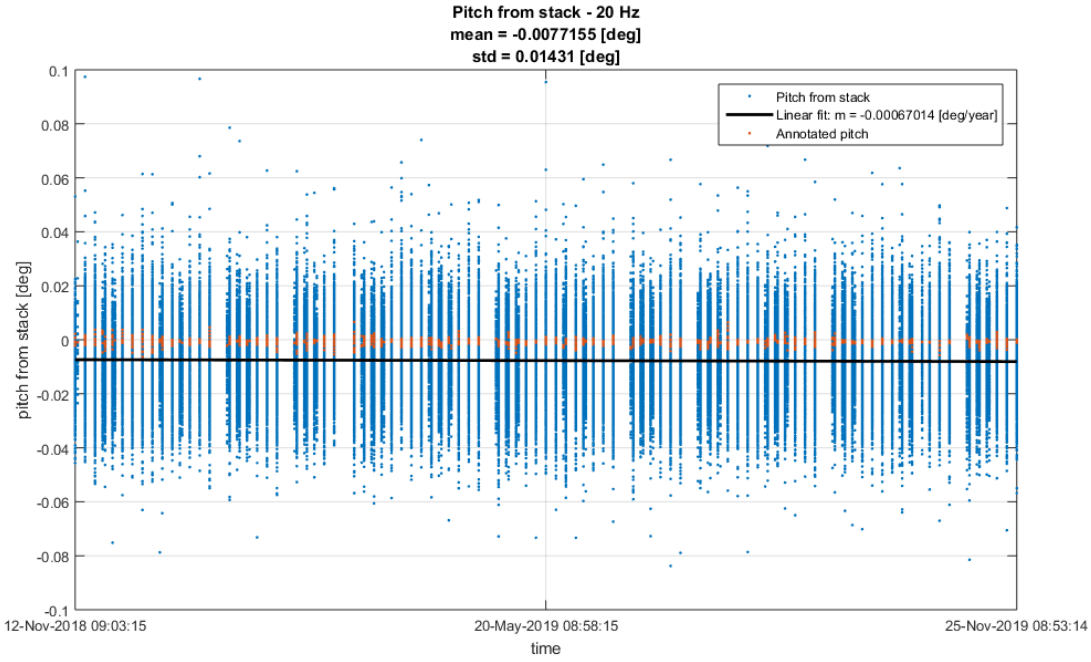

(a)

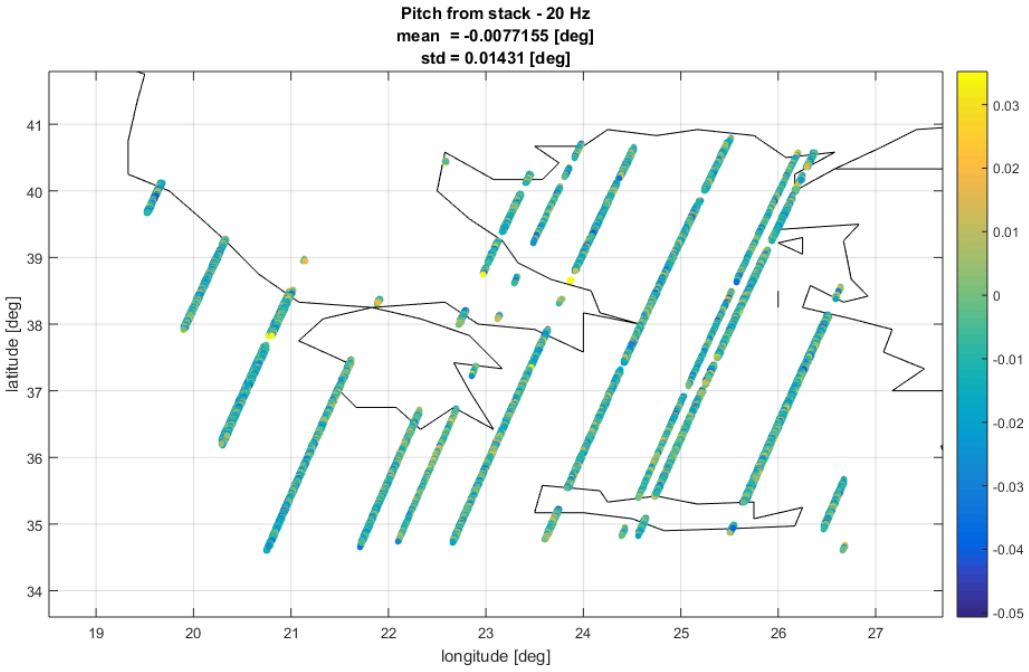

(b)

Figure 30. Pitch from stack estimated from Sentinel-3B descending passes: (a) 20Hz time series and (b) geographical location.

An average pitch bias of -0.0079 degrees has been measured from Sentinel-3B descending passes. The bias seems quite stable in time, with a negligible estimated linear trend of -5.0379e-04 deg/year. The residual variability of the measured bias can be addressed to an incorrect retrieval of the surface slope from the geoid model and to local variations of the dynamically evolving ocean surface. An estimation of the error on the surface slope measurement is provided in Section 4.2.2.

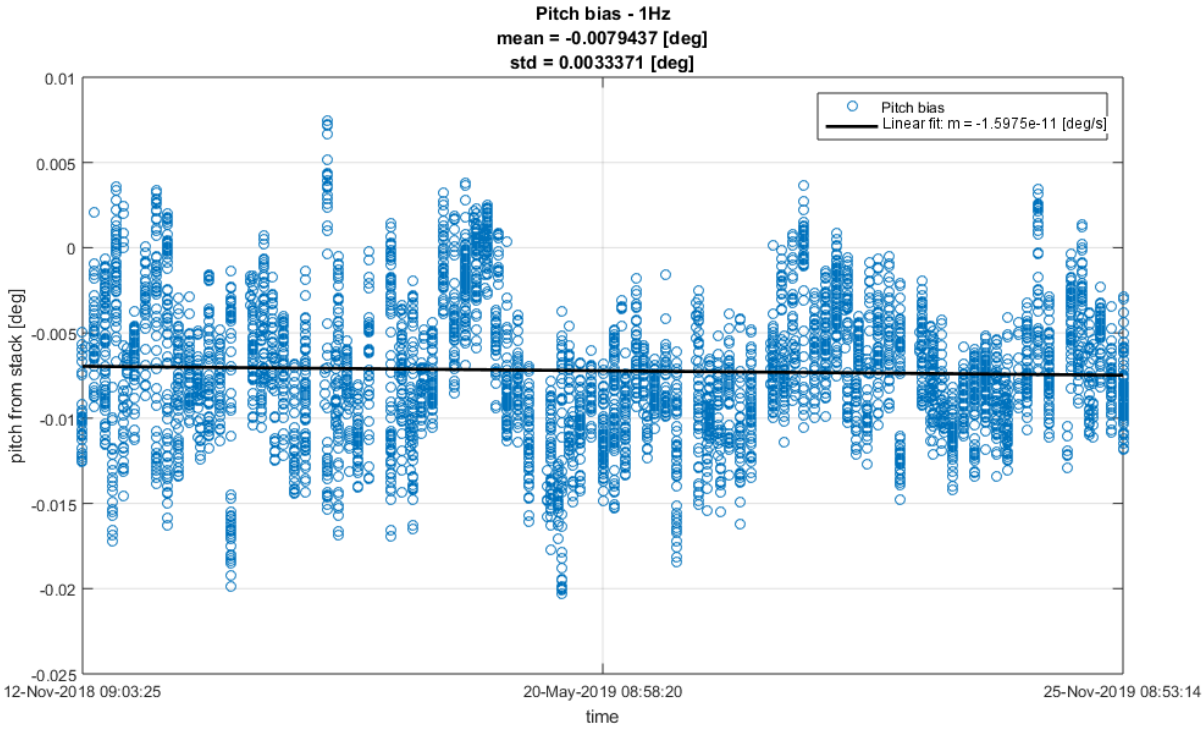

(a)

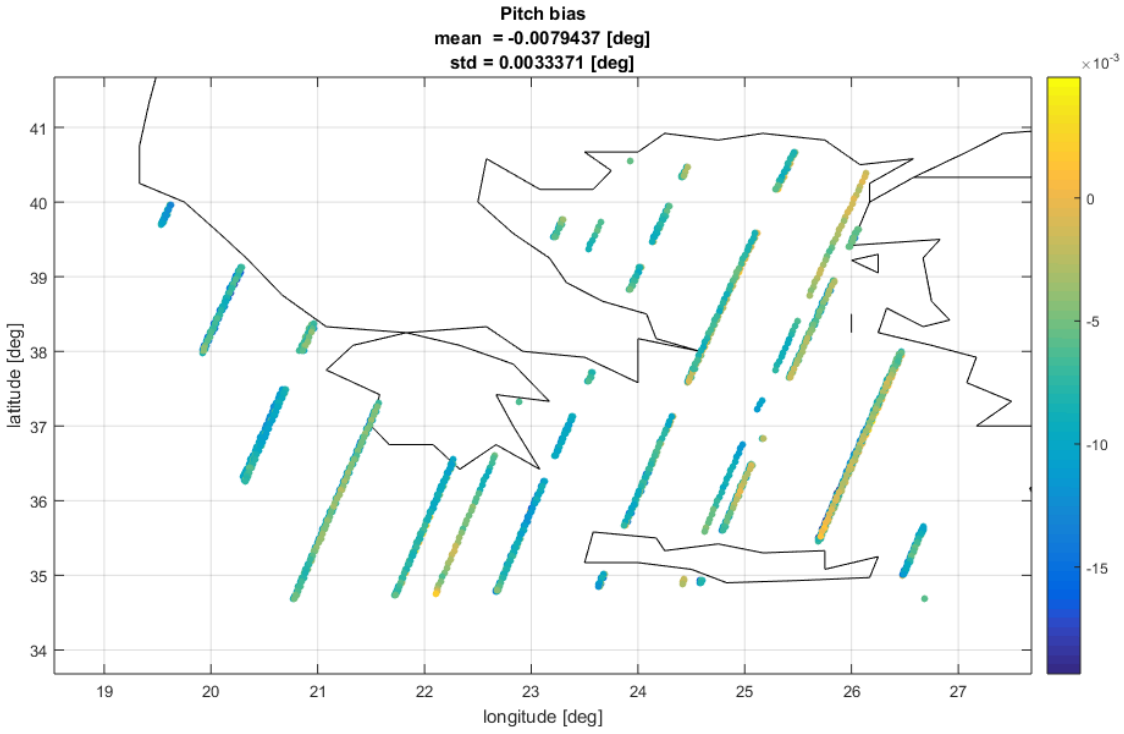

(b)

Figure 31. Pitch bias estimated from Sentinel-3B descending passes: (a) 01Hz time series and (b) geographical location.

3.2.3 Cryosat-2 data analysis

Cryosat-2 L1B Stack data available over Greece has been selected as test dataset. A total of 76 data were available, with acquisition dates ranging from June 2018 to May 2020.
As already noticed for Sentinel-3 data, the estimation converges to two distinct set of values in case of Descending and Ascending passes of the satellite. The two set of data has been consequently analysed separately.

3.2.3.1 Ascending passes

The results obtained from the analysis of the available Cryosat-2 ascending passes are described in this section. Figure 32 (a) provides the time series of the 20-Hz pitch measurements obtained by the stack

processing after the removal of the slope contribution, while Figure 32 (b) provides the same values as function of the geographical locations.

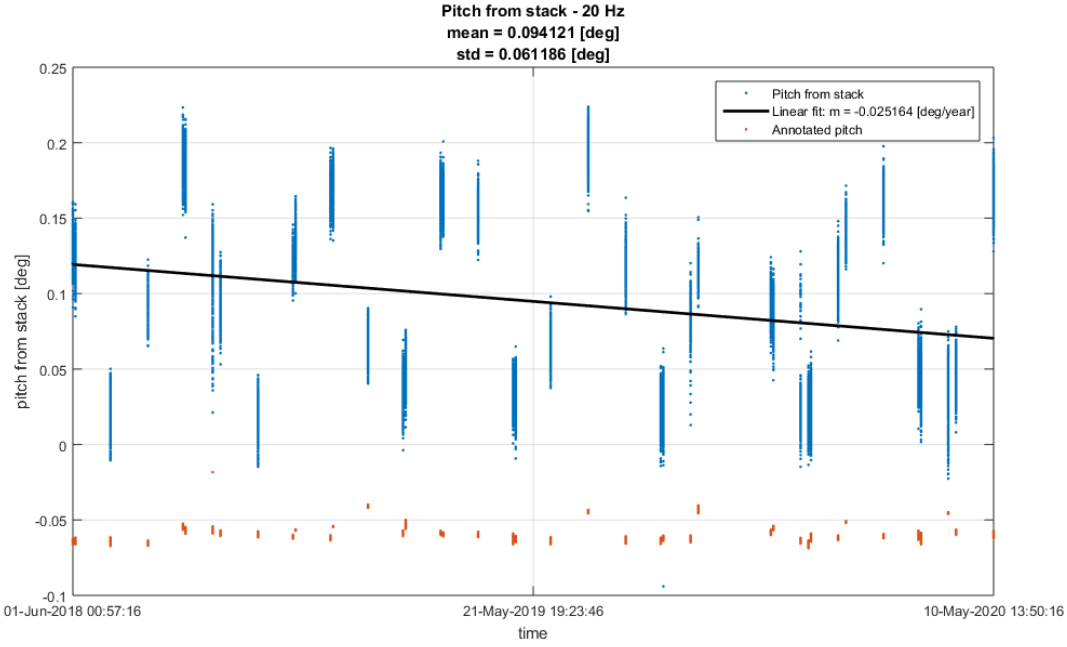

(a)

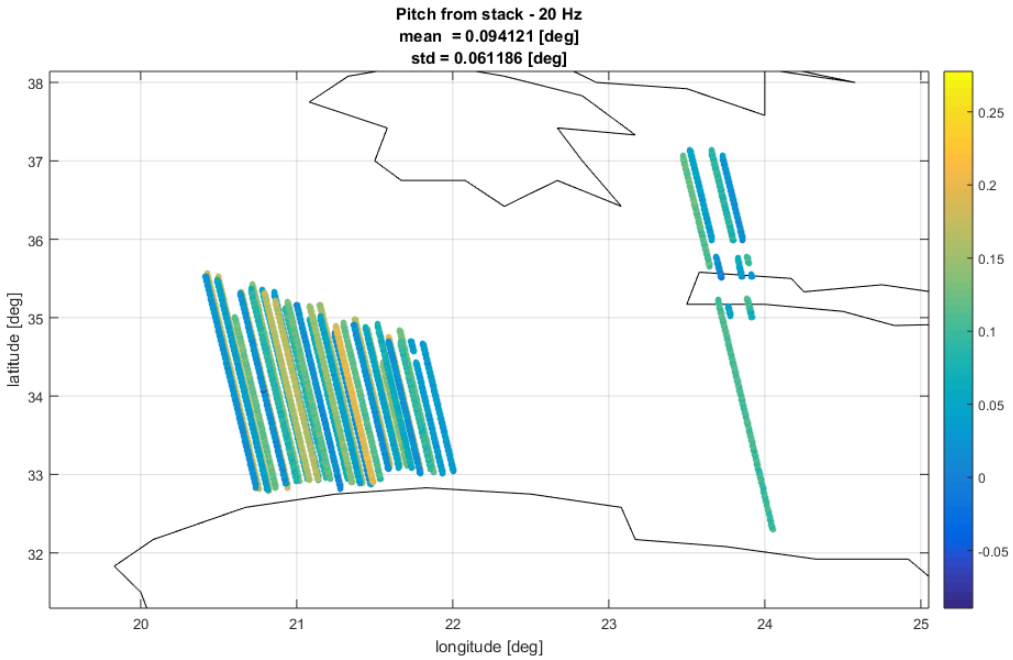

(b)

Figure 32. Pitch from stack estimated from Cryosat-2 ascending passes: (a) 20Hz time series and (b) geographical location.

An average pitch bias of 0.1496 degrees has been measured from Cryosat-2 ascending passes. The bias seems quite stable in time, with a small estimated linear trend of -0.0248 deg/year. The residual variability of the measured bias can be addressed to an incorrect retrieval of the surface slope from the geoid model and to local variations of the dynamically evolving ocean surface. Additional tests have been performed in order to understand the reason for this large pitch bias, with results similar to those shown in Section 3.2.1.1. From the analysis of the stack and of the RIP it is evident that the look angles annotated are quite different in case of ascending and descending passes, thus explaining the different estimates retrieved form the processor. The reason of this difference in the annotated data should be further investigated, and the pitch bias estimated from this dataset reassessed.

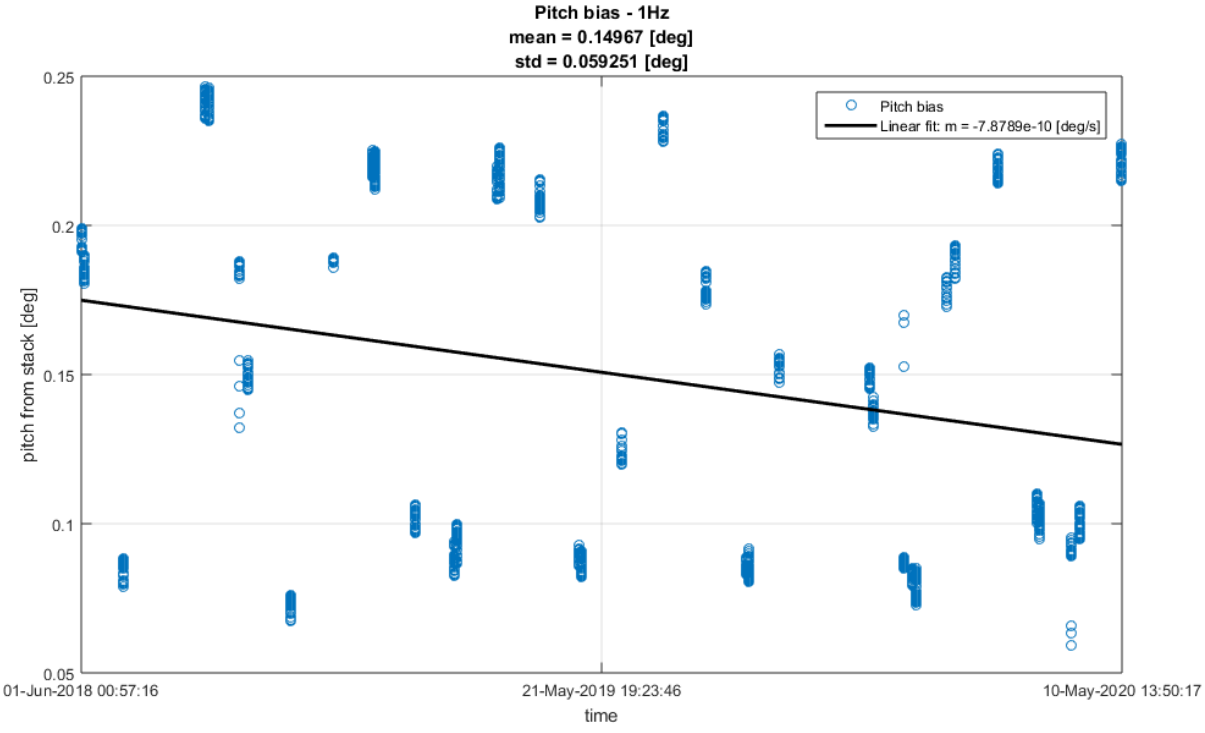

(a)

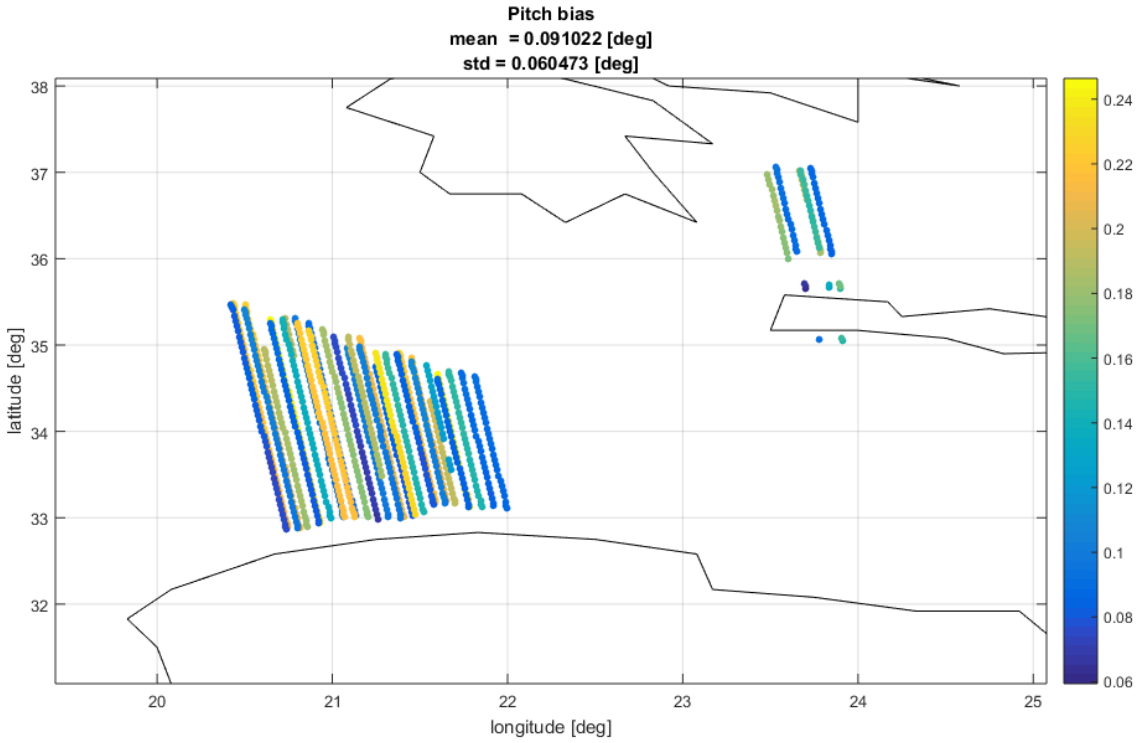

(b)

Figure 33. Pitch bias estimated from Cryosat-2 ascending passes: (a) 01Hz time series and (b) geographical location.

3.2.3.2 Descending passes

The results obtained from the analysis of the available Cryosat-2 descending passes are described in this section. Figure 34 (a) provides the time series of the 20-Hz pitch measurements obtained by the stack processing after the removal of the slope contribution, while Figure 34 (b) provides the same values as function of the geographical locations.

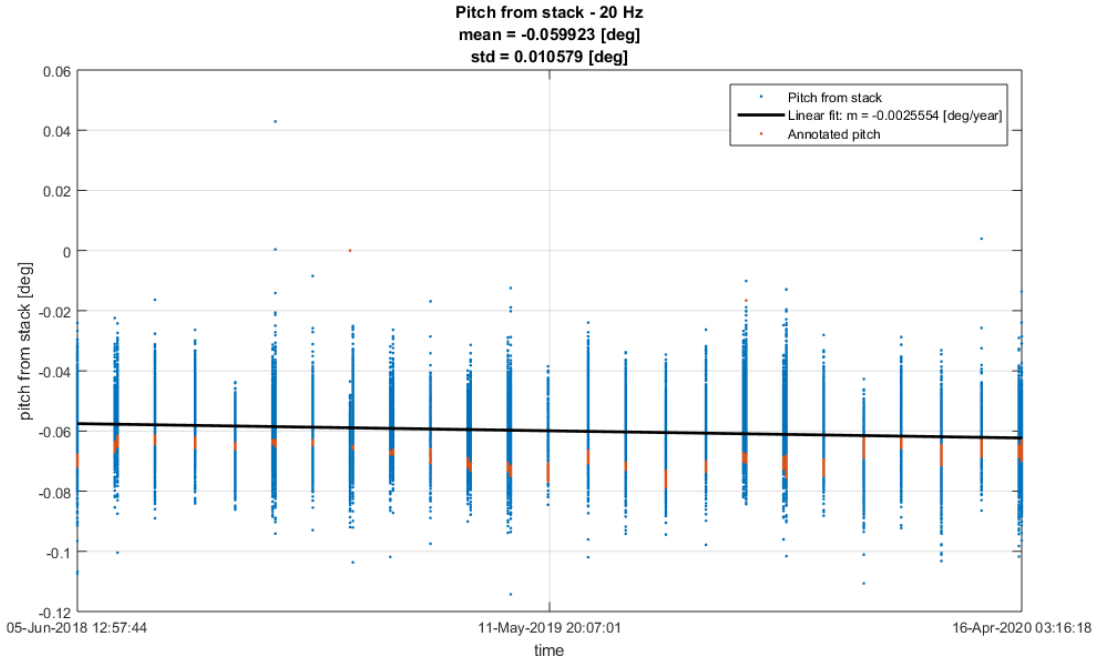

(a)

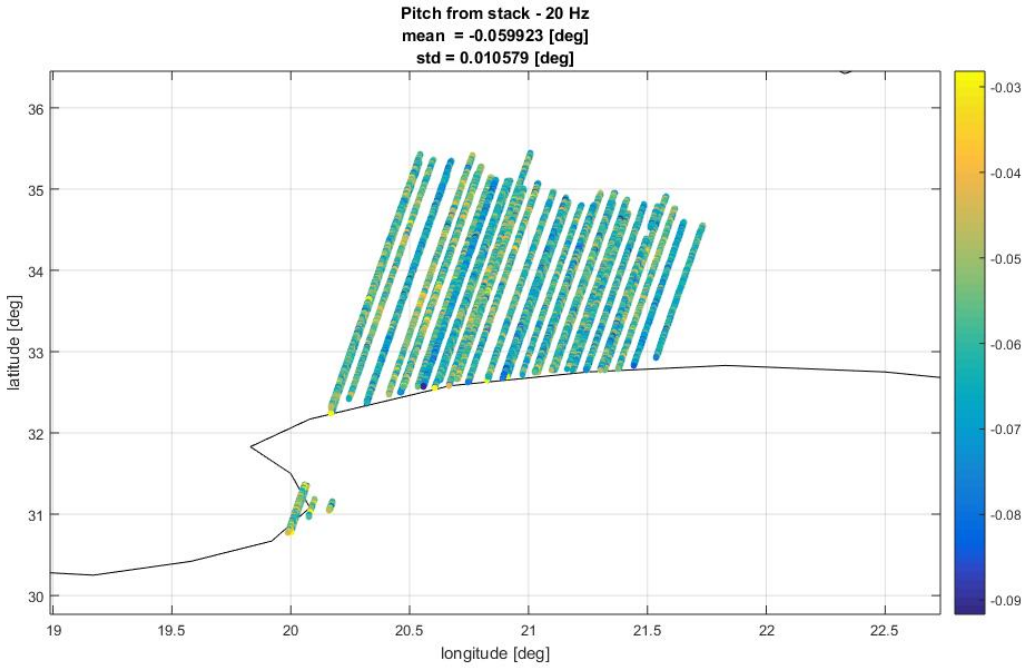

(b)

Figure 34. Pitch from stack estimated from Cryosat-2 descending passes: (a) 20Hz time series and (b) geographical location.

An average pitch bias of 0.0109 degrees has been measured from Cryosat-2 descending passes. The bias seems quite stable in time, with a negligible estimated linear trend of 7.9326e-04 deg/year. The residual variability of the measured bias can be addressed to an incorrect retrieval of the surface slope from the geoid model and to local variations of the dynamically evolving ocean surface. An estimation of the error on the surface slope measurement is provided in Section 4.2.3.

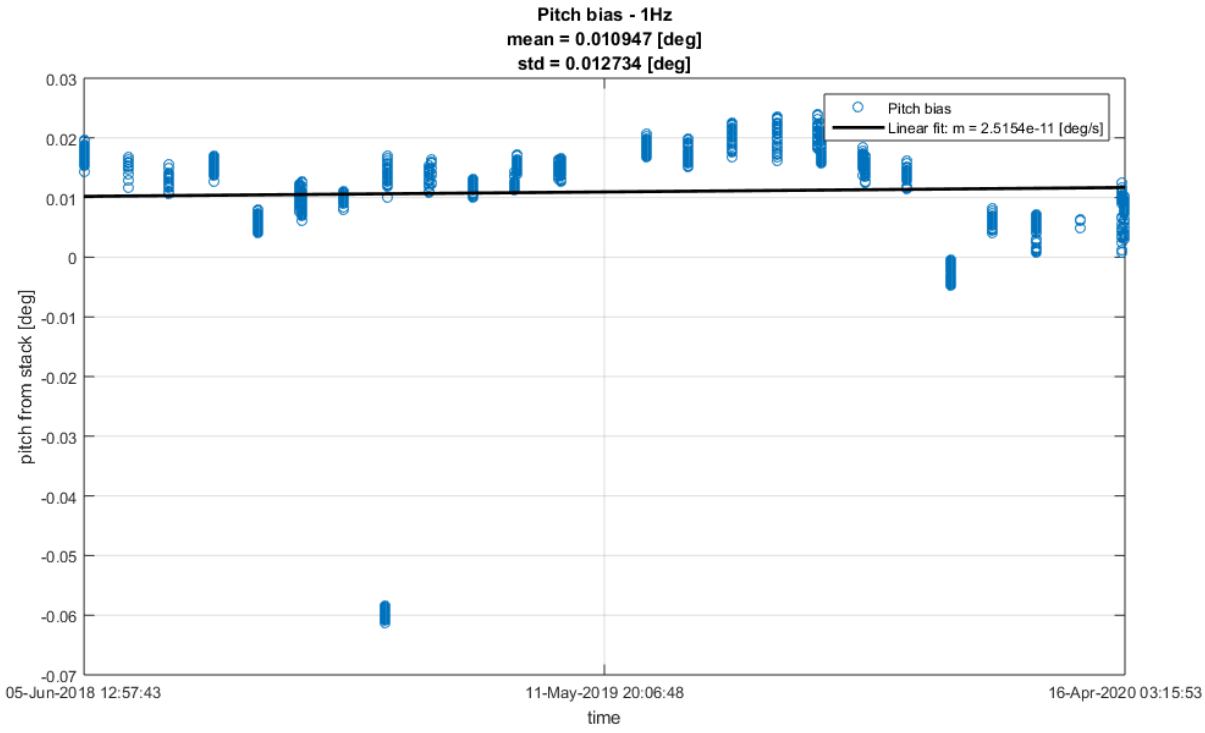

(a)

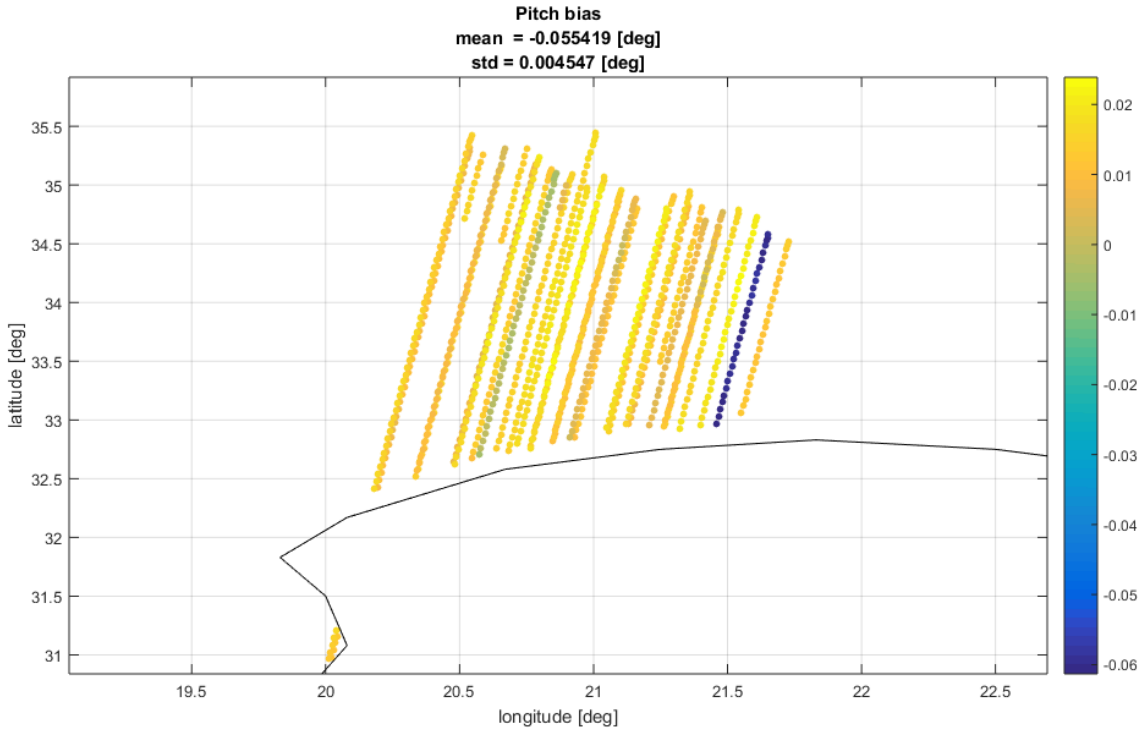

(b)

Figure 35. Pitch bias estimated from Cryosat-2 descending passes: (a) 01Hz time series and (b) geographical location.

4 Processing Case Studies: Along-track / Across-track slope

This section describes the results obtained from the Processors Case studies carried out by Aresys in the framework of WP3130: Along/Across track slope.

4.1 Across-Track slope

As already mentioned in Section 3.1, exploiting the interferometric capability of CryoSat-2, the interferometric phase related to the first arrival of the echo is used to retrieve the angle of arrival of the scattering in the across-track direction. When SIRAL is commanded in SARin mode, the interferometric phase difference between the echoes from the two antennas is used to retrieve the angle of arrival of the first scattering point in the across-track direction. In fact, the across-track echo direction can be derived by exploiting simple geometry and the precise knowledge of the baseline vector (i.e. the vector between the two antennas centres of phase), that depends on the actual antenna mispointing angles. CryoSat-2 interferometric acquisitions over ocean can be exploited to retrieve the across-track slope of the ocean surface [Scagliola et al., 2018]. In the Figure 2.4, the acquisition geometry is sketched.

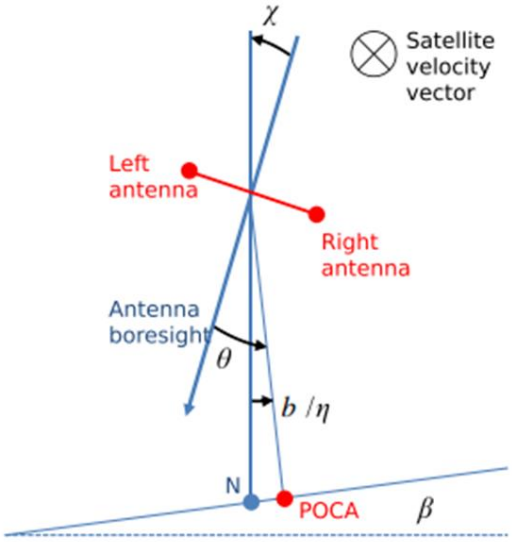

Figure 36. Acquisition geometry in the across-track plane

The interferometer baseline is defined as the versor identifying the direction from the transmitting/receiving antenna phase center (the left antenna) to the receiving only antenna phase center (the right antenna). It is kept in flight orthogonal to the ground track so that the roll angle describes the orientation of the interferometer baseline in the across-track plane. We denote the across-track slope of the ocean surface as and the angle made by the direction of first arrival (i.e. Point of Closest Approach, POCA) with antennas' boresight direction as β. Then, the following relation holds

$$\beta = \eta(\theta - \chi) \qquad \text{Eq. 10.}$$

where η is a geometric factor that is given by $\eta = 1 + h/R$ being h the altitude of the satellite with respect the ellipsoid and R is the Earth's radius.

As already described in Section 3.1, by a priori knowledge of the ocean slope β_{known}, as an example from geoid, it is possible to:

1. assess the end-to-end error on the measured angle of arrival by comparison of the measured slope with β_{known}

$$\epsilon_{e2e} = \theta_m - \chi - \frac{\beta_{known}}{\eta} = a\theta + \epsilon_\theta + \epsilon_\chi + \epsilon_\beta \qquad \text{Eq. 11.}$$

that includes the following error contributions: phase departure $a\theta$, error contribution from the measured angle of arrival ϵ_θ, error contribution from the baselined orientation ϵ_χ and error contribution from the a priori known slope model of the ocean surface ϵ_β. In particular, as described in the following figure, two different approaches have been compared. As first, the approach currently used for the Cryosat interferometer calibration performed during roll campaigns (where the satellite roll is commanded to values of ±0.4 degrees) has been applied to nominal acquisitions with roll close to 0 degrees, as described in Figure 2.5 (a). A simple threshold retracker is used to identify the range samples corresponding to the POCA. The angle of arrival is computed as:

$$\theta_m = \frac{\phi(0)}{k_0 B} \qquad \text{Eq. 12.}$$

where ϕ is the phase difference waveform, evaluated in correspondence of delay equal to 0, i.e. in the POCA. Conversely, a new method has been implemented (see Figure 2.5 (b)) that makes use of Aresys in-house physical retracker to obtain from the SSH a more reliable estimate of the range samples corresponding to the POCA. Additionally, the SWH is exploited in order to obtain an estimation of the phase departure term, according to the following model:

$$\varphi_d(\theta, \sigma_s) = \mathrm{a}(\sigma_s)\theta = [a_0(1 + b\sigma_s^2 + d\sigma_s^4)]\theta \qquad \text{Eq. 13.}$$

Where the coefficients are $a_0 = -0.0305$, $b = 0.384m^{-2}$ and $d = -0.024m^{-4}$.

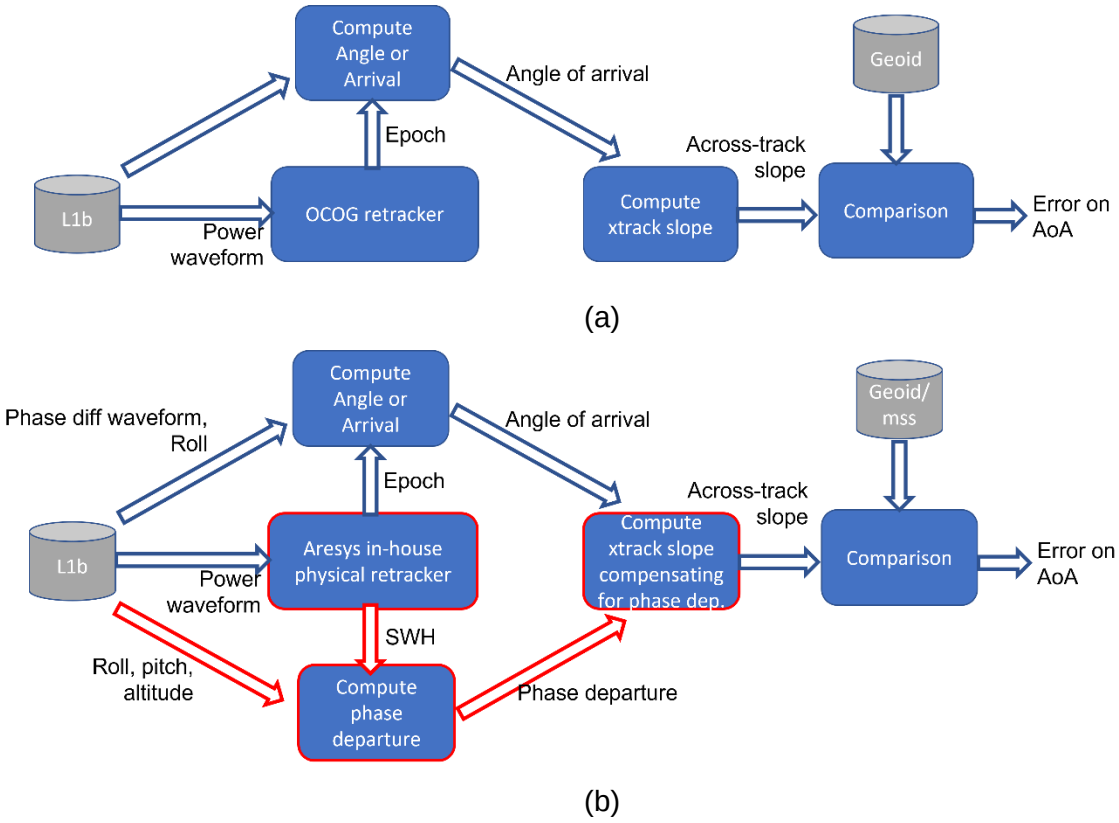

Figure 37. Different approaches for the computation of the AoA error.

2. Compute a calibration function (e.g. linear model)

$$F(\theta) = a\theta + \chi_0 \quad \text{Eq. 14.}$$

where the linear term a provides an estimate of the phase departure, while the constant term χ_0 provides an estimate of the bias affecting the roll.

3. Assess the residual error on the measured angle of arrival after application of the calibration function

$$\epsilon_r = \frac{\theta_{L1b}}{1+a} - (\chi - \chi_0) - \frac{\beta_{known}}{\eta} \quad \text{Eq. 15.}$$

This quantity, after the removal of the estimated roll bias, represents the residual error on the knowledge of the surface slope.

4. Compute the performance of the method in terms of residual across-track slope accuracy and precision, according to the following definitions: accuracy is the median of the absolute errors for different acquisitions while the precision is the median of standard deviation of errors for different acquisitions.

Aresys has exploited CryoSat-2 SARin acquisitions over sea aiming at retrieving the across-track slopes of the surface exploiting the relation above and by including further corrections to the measured angle of arrival. In particular, from experience in the calibration of the CryoSat-2 interferometer, it has been verified that the compensation of the phase departure [Scagliola et al., 2018] is crucial to obtain an increased accuracy of the across-track slopes. It is worth recalling that a proof of concept for this approach was already presented in [Galin et al., 2013].

4.1.1 Cryosat-2 roll campaigns data analysis

The results obtained by testing the different configurations in case of Cryosat-2 roll campaign data are presented in this section. For more details on the analyzed dataset and on the different configurations teste please refer to Section 3.1.1.

The following figure presents the comparison between the estimated residual across-track slope accuracy and precision for the analysed configurations.

Figure 38 (a) provides a comparison of the residual across-track slope accuracy estimated from the residual error measured on the angle of arrival after the calibration function compensation. It can be noticed that all the analyzed cases provide similar values for the estimated residual accuracy, with a mean value of 12.48 microrad.

Figure 38 (b) provides a comparison of the residual across-track slope precision estimated from the residual error measured on the angle of arrival after the calibration function compensation. It can be noticed that all the analyzed cases provide similar values for the estimated residual precision, with a mean value of 27.19 microrad. The case with physical retracker and no compensation of the phase departure term shows a small increase in the standard deviation. This might be due to inaccuracies in the POCA location estimation which needs to be further investigated.

(a)

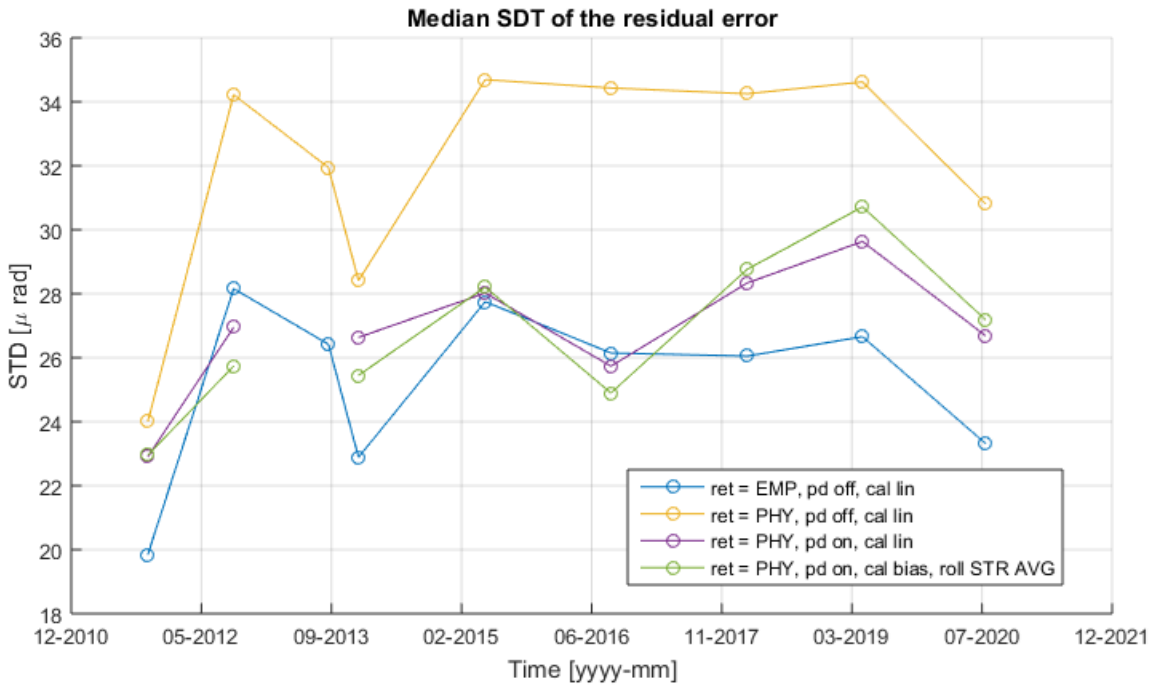

(b)

Figure 38. Results from Cryosat-2 roll campaigns analysis: Across track slope accuracy (a) and precision (b).

4.1.2 Cryosat-2 nominal acquisitions data analysis

The results obtained by testing the different configurations in case of Cryosat-2 L1B acquisitions over Greece are presented in this section. For more details on the analyzed dataset and on the different configurations teste please refer to Section 3.1.2.

The following figure presents the comparison between the estimated residual across-track slope accuracy and precision for the analysed configurations.

Figure 39 (a) provides a comparison of the residual across-track slope accuracy estimated from the residual error measured on the angle of arrival after the calibration function compensation. It can be noticed that all the analyzed cases provide similar values for the estimated residual accuracy, with a mean value of 18.41 microrad.

Figure 39 (b) provides a comparison of the residual across-track slope precision estimated from the residual error measured on the angle of arrival after the calibration function compensation. It can be noticed that all the analyzed cases using the empirical retracker provide similar values for the estimated

residual precision, with a mean value of 32.65 microrad. The cases where the physical retracker has been used show a small increase in the standard deviation, with an average value of 40.6 microrad. This might be due to inaccuracies of the retracker in the estimation of the POCA location in the coastal area analyzed.

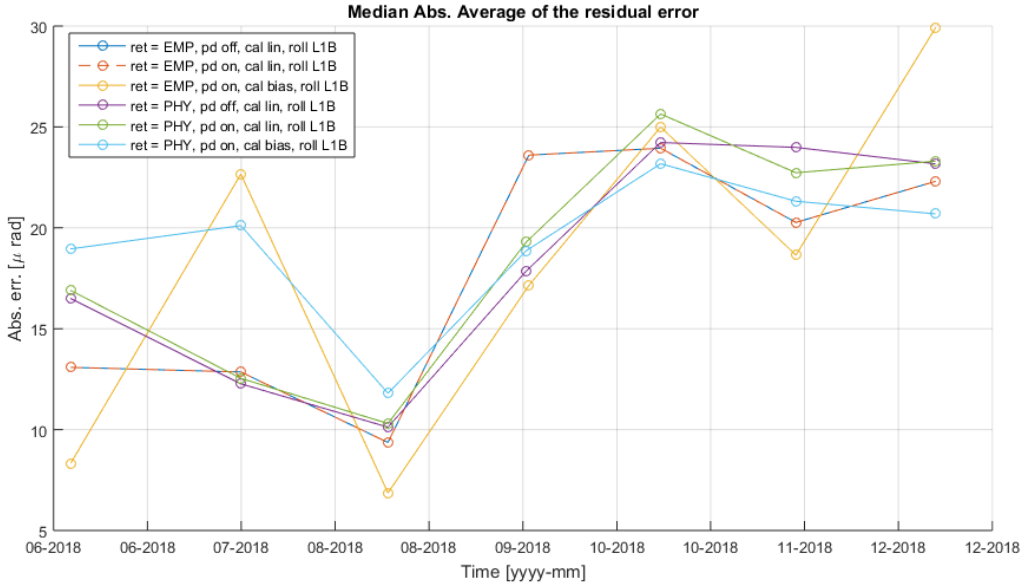

(a)

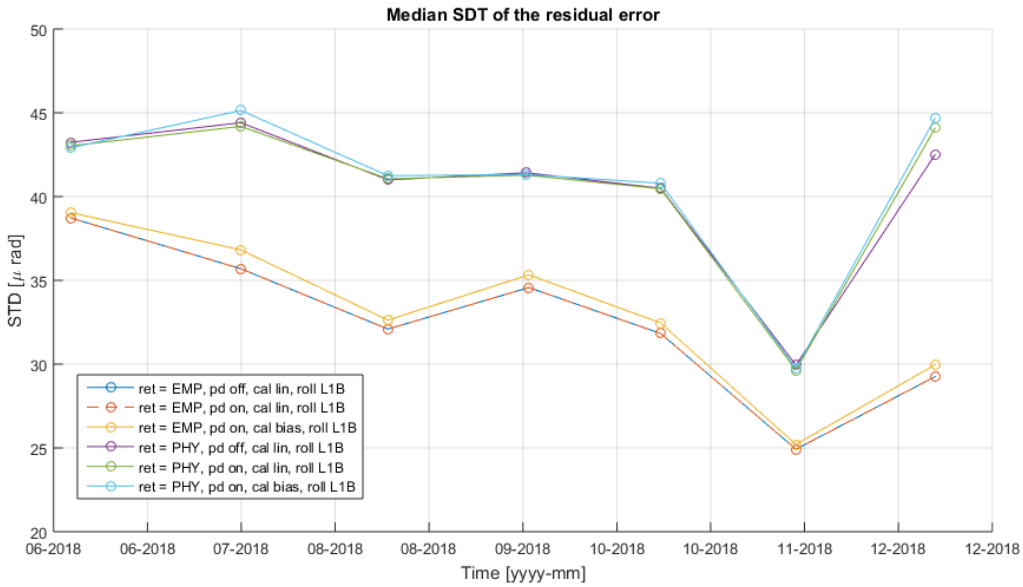

(b)

Figure 39. Results from Cryosat-2 data over Greece analysis: Across track slope accuracy (a) and precision (b).

4.2 Along-Track slope

Recalling that on a uniformly rough spherical surface, e.g., the ocean, the power of the single-look echoes in a surface sample stack is modulated by the along-track antenna pattern, the look angle for a given surface sample is here defined as the angle at which the surface sample itself is seen with respect to the nadir direction.

Recalling that the antenna gain pattern in is approximately separable into its along- and across-track components, the power of the single-look echoes can be written as a function of the delay τ and of the look angle ξ as

$$X(\tau,\xi) = A\ exp\left[-\frac{2(\xi-\mu-\frac{\varsigma}{\eta})}{\gamma_1^2}\right] \quad \text{Eq. 16.}$$

where the first term A is a constant, $F(\ \ )$ denotes a function of the delay (including the across-track antenna pattern), and the second term is the power gain given by the along-track antenna pattern as a function of the look angle ξ, the pitch μ, and the along-track component of the surface vector gradient scaled by a geometrical factor ς/η. It has to be remarked here that in the formula above the unknown ς/η is summed with the pitch, as a consequence an accurate knowledge of the surface slope is needed to retrieve the pitch estimates with sufficient accuracy. The proposed method to derive the along-track component of the surface vector ς as the only inputs the stack of single-look echoes and the look angle associated to each echo. Starting from those inputs, the following quantities are sequentially computed:

1. Power of the single-look echo
2. Integration in time delay: The power distribution as a function of the look angle only is computed by integrating the power stack for the time delay corresponding to the leading edge. Since the leading edge of the echo corresponds to the along-track strip at the nadir of the instrument, so aiming at avoiding the dependence on the across-track pattern, it is reasonable in to sum only the power contributions from the leading edge.
3. Along-track antenna pattern fitting: Nonlinear least square fitting is used to estimate the location of the maximum of the antenna pattern.

The proposed method returns values at 20 Hz frequency, i.e., one for each surface sample; anyway, those measurements are expected to be affected by noise. The values retrieved at 20 Hz can be averaged at 01Hz to increase the accuracy of the estimate.

Following the estimation of the 20Hz values of the pitch from the L1BS data, the procedure described in the following figure is applied in order to obtain an estimation of the error affecting the surface slope.

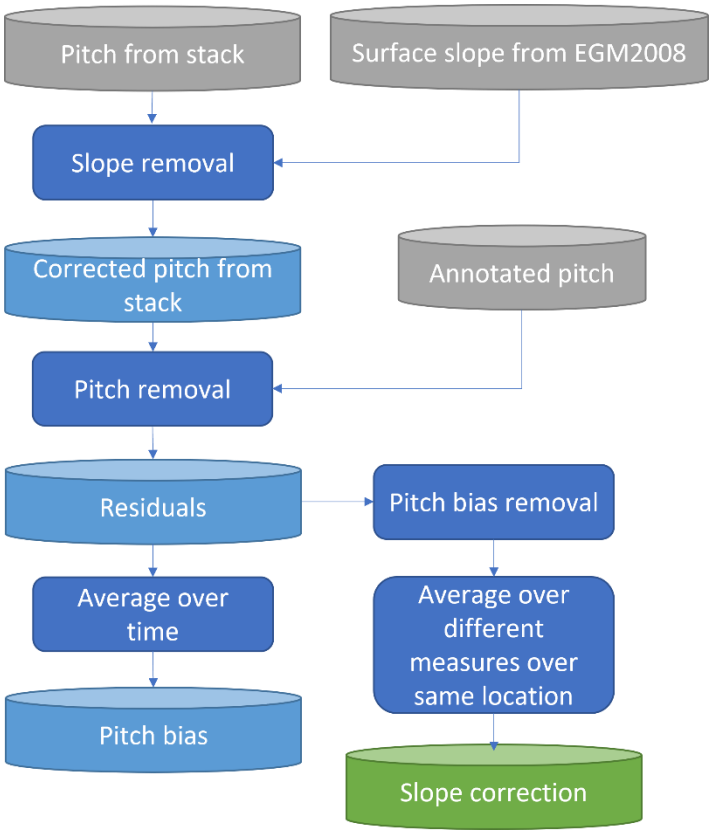

Figure 40. Pitch bias estimation: processing steps.

The measurements obtained from the L1BS stack, i.e. the look angle associated to the maximum of the antenna pattern fitted to the RIP, consists in the sum of the contributions of:

- The pitch angle of the satellite;
- The along track slope of the surface;

The first steps of the procedure have been already described di Section 3.2. Starting from the residuals computed by removing from the pitch from stack the contributions of the slope form the geoid and the pitch annotated in the data, the estimated pitch bias is removed. Finally, whenever possible, different measures of the residuals over the same geographical locations are averaged, in order to remove time dependent contributions and obtain an estimation of the correction to be applied to the slope retrieved form the geoid.

In the following sections, the results obtained from the analysis of the Sentinel-3A, Sentinel-3B and Cryosat-2 datasets over Greece are presented.

4.2.1 Sentinel-3A data analysis

4.2.1.1 Ascending passes

The results obtained from the analysis of the available Sentinel-3A ascending passes are described in this section.

Figure 41 (a) provides the 01-Hz along track slope measurements retrieved from the geoid model, while Figure 41 (b) provides the slope corrections estimated from the stack processing after the removal of the pitch contribution. It can be noticed that the estimated correction values are an order of magnitude greater than the slope retrieved from the geoid and present a strong dependence on the latitude. This further suggest that the dataset is further analysed following some investigation on the anomalies in the input data.

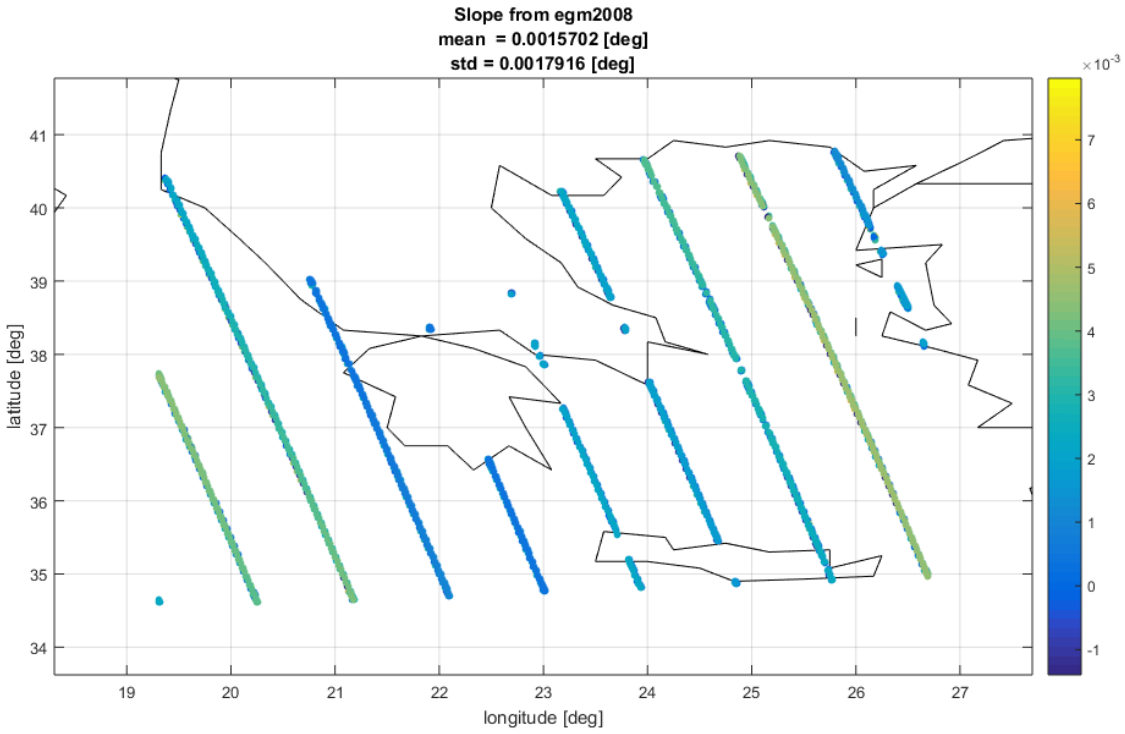

(a)

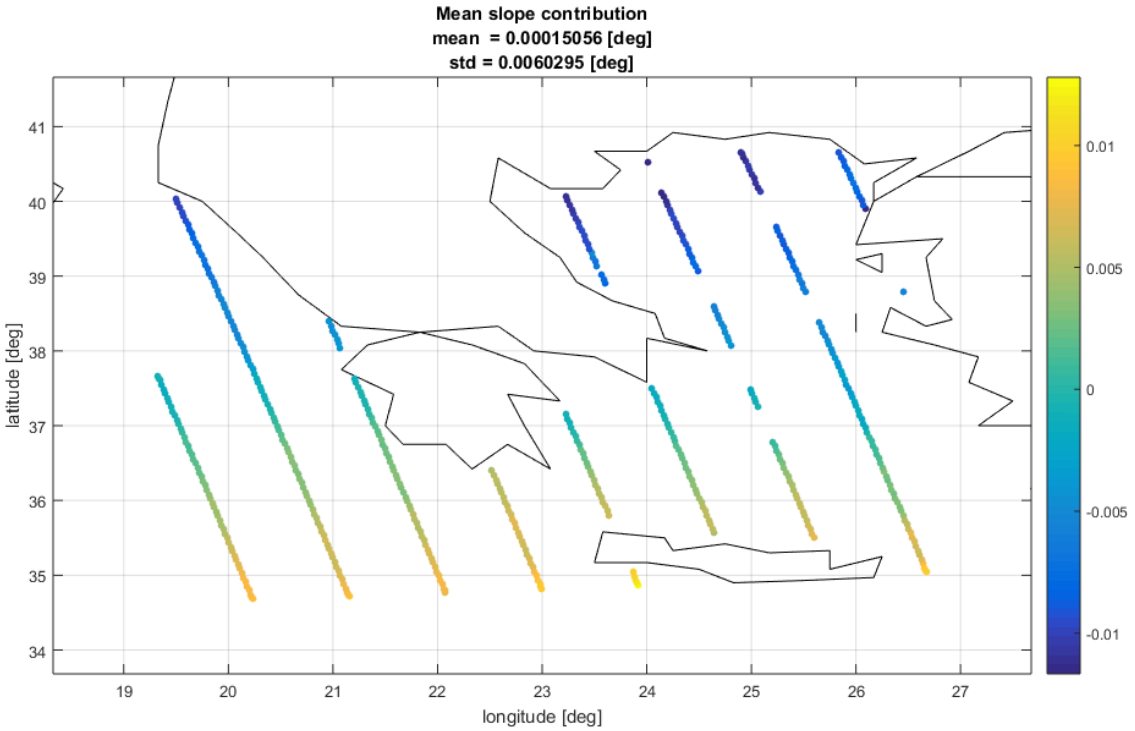

(b)

Figure 41. Results from Sentinel-3A ascending passes: (a) 01Hz along-track slope from geoid and (b) 01Hz along-track slope correction from stack processing.

4.2.1.2 Descending passes

The results obtained from the analysis of the available Sentinel-3A descending passes are described in this section.

Figure 42 (a) provides the 01-Hz along track slope measurements retrieved from the geoid model, while Figure 42 (b) provides the slope corrections estimated from the stack processing after the removal of the pitch contribution.

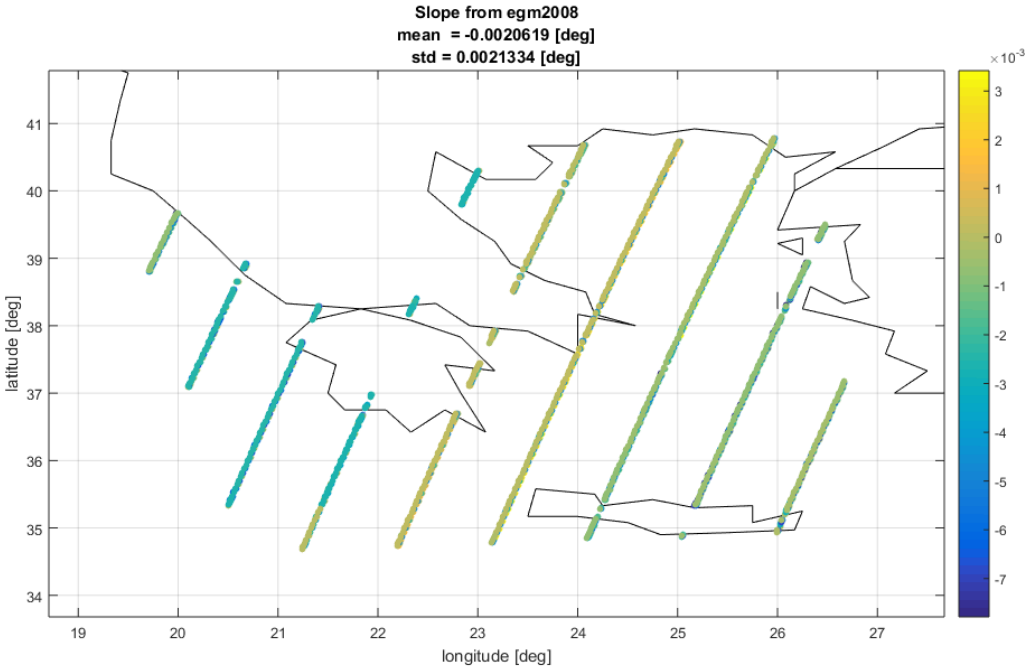

(a)

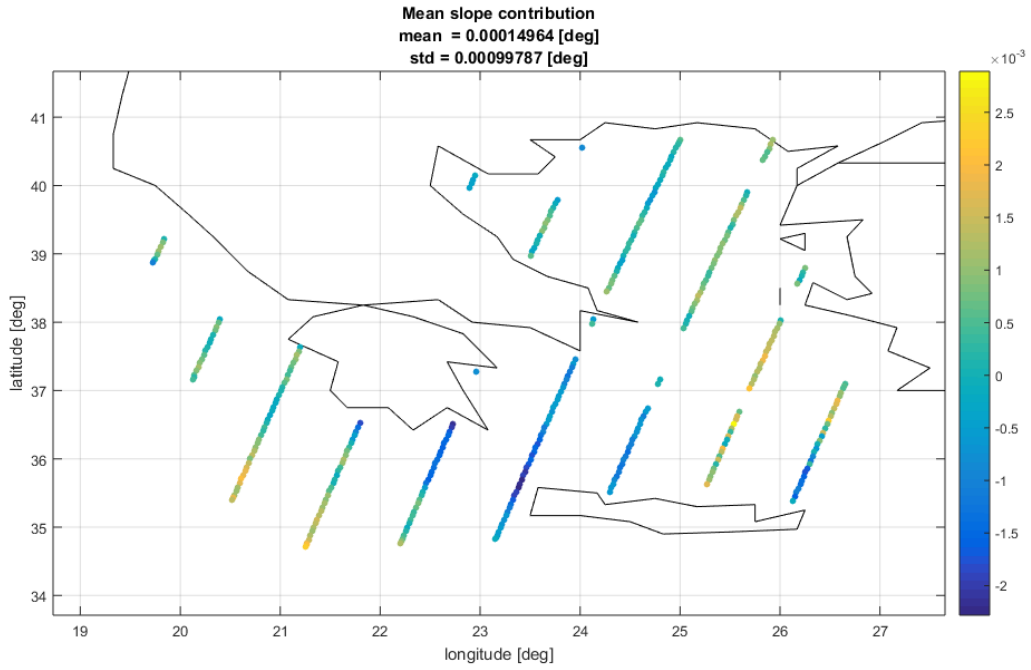

(b)

Figure 42. Results from Sentinel-3A descending passes: (a) 01Hz along-track slope from geoid and (b) 01Hz along-track slope correction from stack processing.

4.2.2 Sentinel-3B data analysis

4.2.2.1 Ascending passes

The results obtained from the analysis of the available Sentinel-3B ascending passes are described in this section.

Figure 43 (a) provides the 01-Hz along track slope measurements retrieved from the geoid model, while Figure 43 (b) provides the slope corrections estimated from the stack processing after the removal of the pitch contribution. It can be noticed that the estimated correction values are an order of magnitude greater than the slope retrieved from the geoid and present a strong dependence on the latitude. This further suggest that the dataset is further analysed following some investigation on the anomalies in the input data.

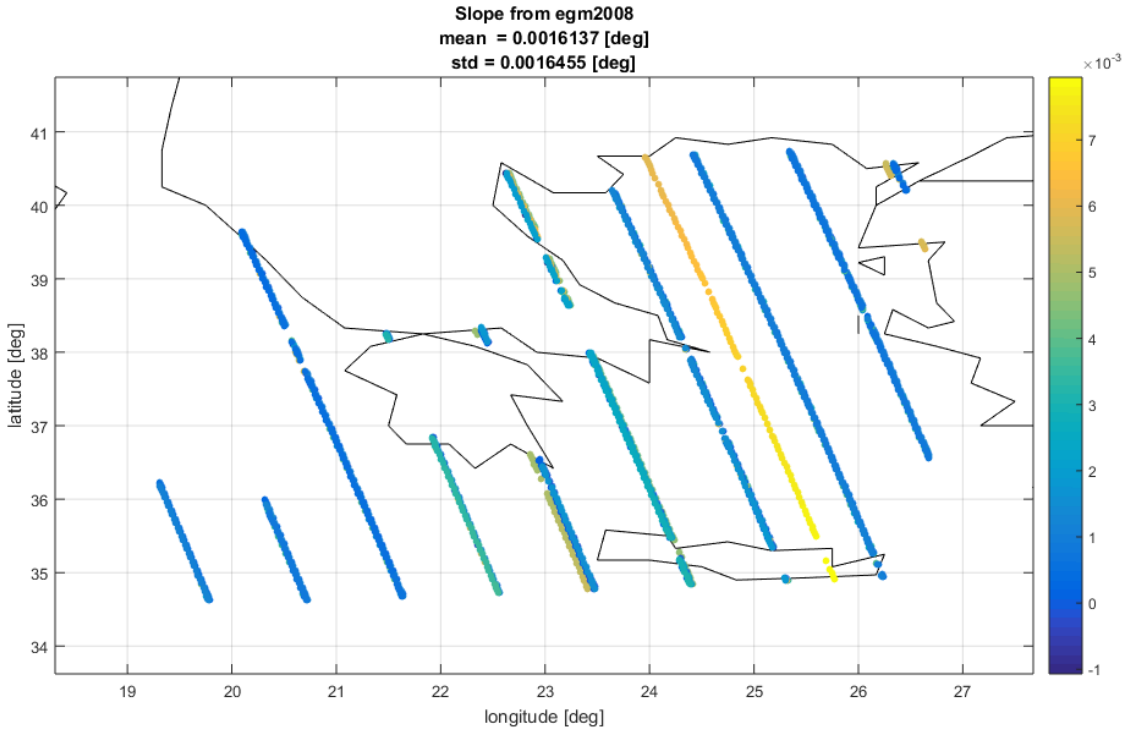

(a)

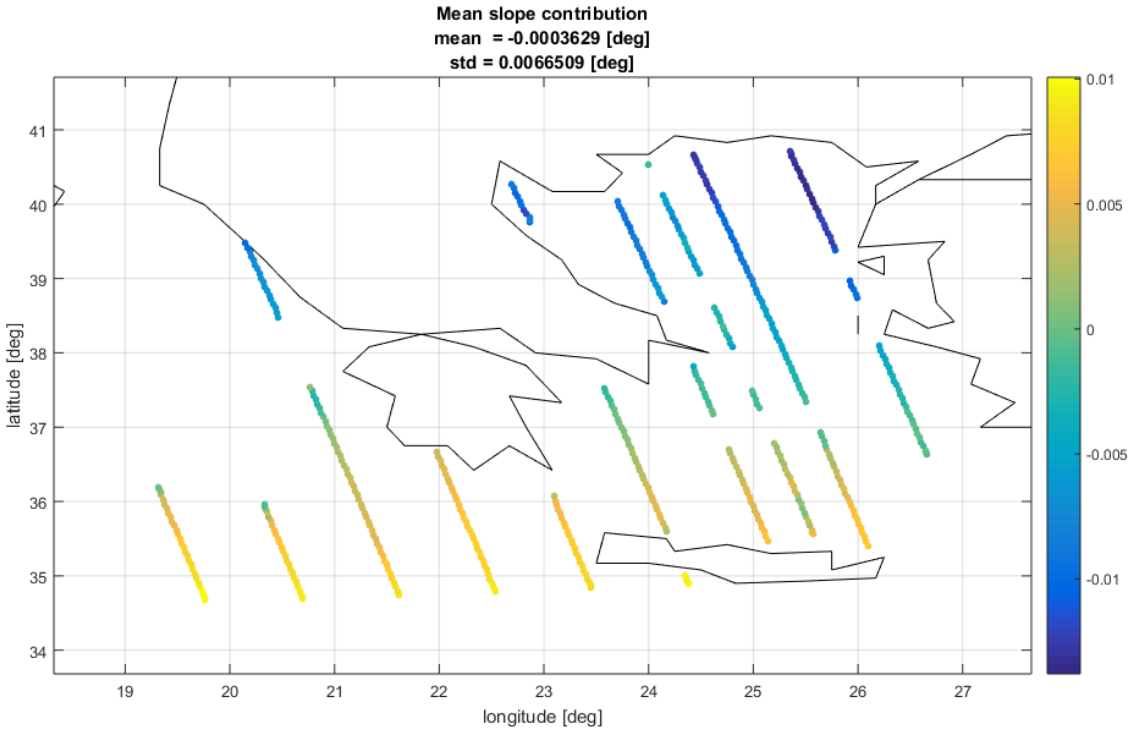

(b)

Figure 43. Results from Sentinel-3B ascending passes: (a) 01Hz along-track slope from geoid and (b) 01Hz along-track slope correction from stack processing.

4.2.2.2 Descending passes

The results obtained from the analysis of the available Sentinel-3B descending passes are described in this section.

Figure 44 (a) provides the 01-Hz along track slope measurements retrieved from the geoid model, while Figure 44 (b) provides the slope corrections estimated from the stack processing after the removal of the pitch contribution.

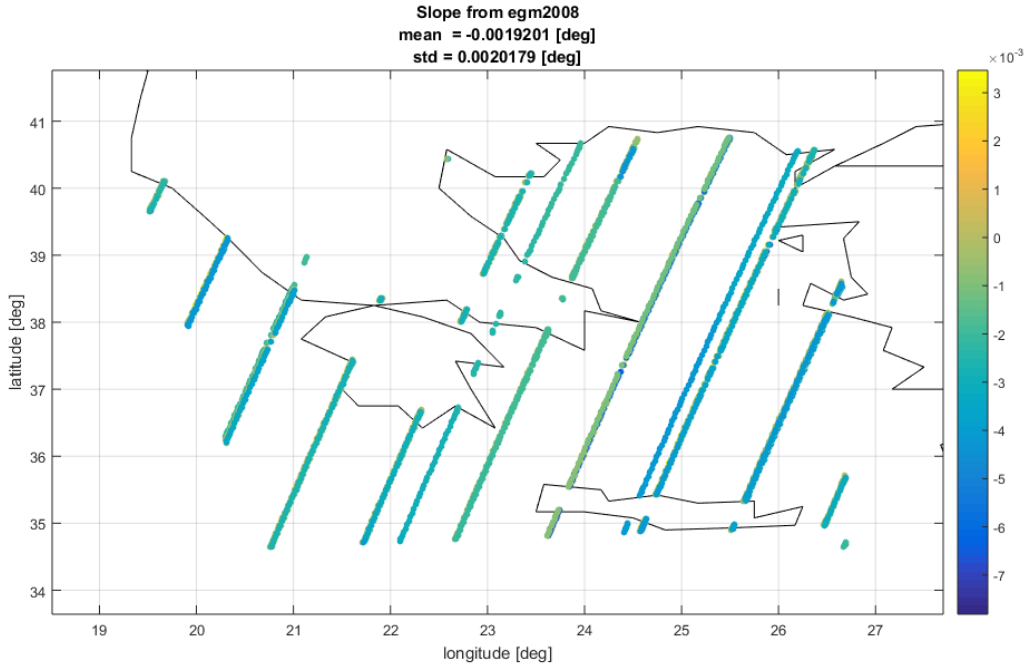

(a)

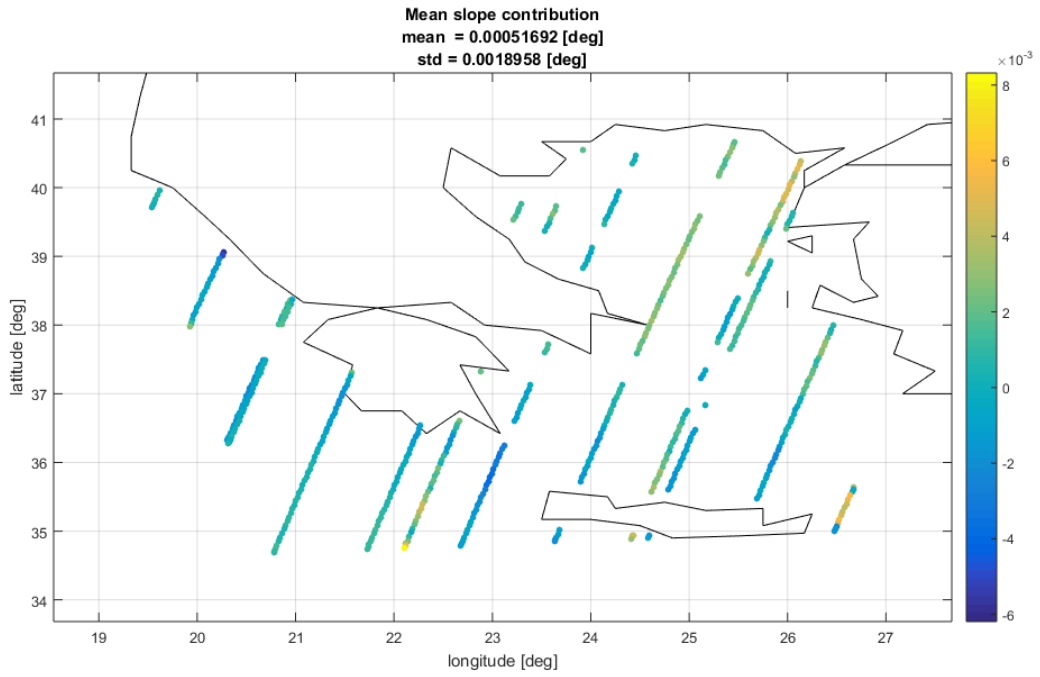

(b)

Figure 44. Results from Sentinel-3B descending passes: (a) 01Hz along-track slope from geoid and (b) 01Hz along-track slope correction from stack processing.

4.2.3 Cryosat-2 data analysis

4.2.3.1 Descending passes

The results obtained from the analysis of the available Cryosat-2 descending passes are described in this section.

Figure 45 (a) provides the 01-Hz along track slope measurements retrieved from the geoid model, while Figure 45 (b) provides the slope corrections estimated from the stack processing after the removal of the pitch contribution. It is worth noticing that for Cryosat-2 data, due to the different orbit with respect to the Sentinel-3 case, it was not possible to average different measures over the same location. For this reason, several more data over time should be analyzed in order to provide a reliable estimation of the slope correction.

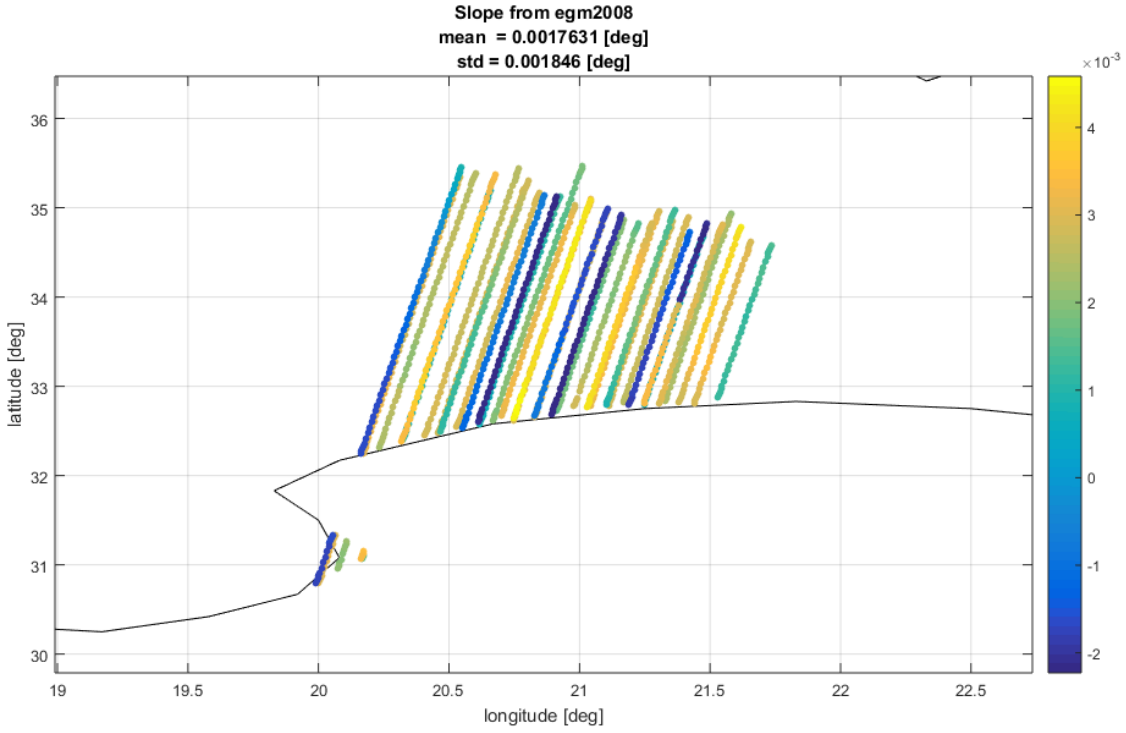

(a)

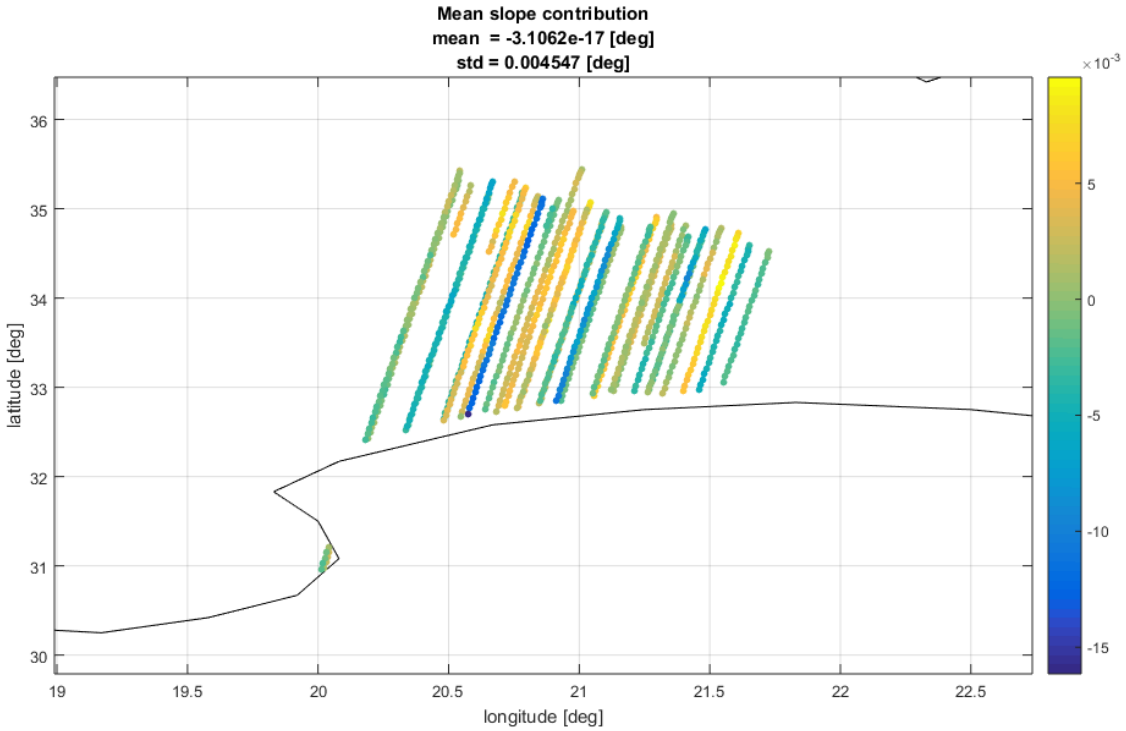

(b)

Figure 45. Results from Cryosat-2 descending passes: (a) 01Hz along-track slope from geoid and (b) 01Hz along-track slope correction from stack processing.

5 Summary

This section provides a summary of the main results and final recommendations for the analyzed case studies.

Section 2 present an overview of the FFSAR processing in the frequency domain. The optimal multi-looking step has been investigated to trade-off between the along-track sampling of the waveforms and the speckle reduction, which is particularly of interest in the coastal zone. A theoretical model that describes the standard deviation reduction as a function of the number of samples averaged together has been presented and a practical procedure to select the multilooking step in function of the desired reduction in the noise standard deviation has been proposed. Additionally, an overview on the issue of the grating lobes affecting FFSAR waveforms has been provided and a characterization of the main contributing effects has been given in case of Cryosat-2 and Sentinel-3 missions, along with examples from simulated and real data. This effect is particularly visible on inland bodies. A method for the grating-lobes mitigation in case of closed-burst acquisition mode has been proposed and tested over simulated data.

The analysis of L1B SARIn Cryosat-2 data roll campaigns (see Section 3.1) allowed to retrieve an estimation of the bias affecting the roll. The estimated roll bias is -0.1145 degrees, with a slightly increasing trend of -53.85 mdeg/year. An estimation of the roll bias has been attempted also from the analysis of the available acquisitions over Greece, where the satellite is not rolled. It is worth noticing that, for these analyses, the compensation of the known roll has been performed starting from the attitude annotated in the L1B input files, where the known roll bias has already been compensated. This explains the different bias estimated with respect to the roll campaigns case. Additionally, it is remarked that, while the average acquisition length in case of roll campaigns is of ~10 minutes, the available dataset over Greece is composed of passes with average duration of ~2 minutes with several cases of land contamination. In order to fully validate the newly proposed approach applicability in case the satellite is not rolled, longer acquisitions should be analyzed in open ocean areas away from the coast.

The analysis of L1B SARIn Cryosat-2 data roll campaigns (see Section 4.1) allowed to retrieve an estimation of the residual across-track slope accuracy (mean value of 12.48 microrad) and precision (27.19 microrad).

The analysis of L1B stack data (see Section 3.2) allowed to retrieve an estimation of the bias affecting the pitch annotated in the L1BS product. The outcomes of the analysis are summarized in the following table. Please note that only descending passes have been included in the analysis, since a discrepancy in the look angles annotated in the L1BS products have been identified in case of ascending passes. The

reason of this difference in the annotated data should be further investigated, and the pitch bias and along-track surface slope correction estimated from this dataset reassessed.

Mission	Pitch bias mean [deg]	Pitch bias standard deviation [deg]
Sentinel-3A	0.0088	0.0034
Sentinel-3B	-0.0079	0.0033
Cryosat-2	0.0109	0.0127

Additionally, after removing the pitch bias, an estimation of the error affecting the along-track surface slope model has been attempted. The mean slope correction and the related standard deviations are summarized in the following table for the analyzed data over Greece. The high values of standard deviation can be partly addressed to the local variability of the surface slope in the analyzed area, but still suggests the opportunity to extend the time period of the analysis in order to have a higher number of passes over the same location. This would allow to effectively remove the variability due to time-dependent sea state conditions. It is worth noticing that for Cryosat-2 data, due to the different orbit with respect to the Sentinel-3 case, it was not possible to average different measures over the same location. For this reason, several more data over time should be analyzed in order to provide a reliable estimation of the slope correction, as suggested by the high standard deviation.

Mission	Slope correction mean [deg]	Slope correction standard deviation [deg]
Sentinel-3A	0.00015	0.00099
Sentinel-3B	0.00051	0.00189
Cryosat-2	-3.1e-17	0.00454

6 References

Egido A. and W. H. F. Smith, (2017) "Fully Focused SAR Altimetry: Theory and Applications," in IEEE Transactions on Geoscience and Remote Sensing, vol. 55, no. 1, pp. 392-406, Jan. 2017.

[Ehlers et al., 2022] Ehlers, F., Schlembach, F., Kleinherenbrink, M., and Slobbe, C. (2022). Validity assessment of SAMOSA retracking for fully-focused SAR altimeter waveforms. Advances in Space Research.

Galin N., , D. J. Wingham, R. Cullen, M. Fornari, W. H. F. Smith and S. Abdalla, (2013) "Calibration of the CryoSat-2 Interferometer and Measurement of Across-Track Ocean Slope," in IEEE Transactions on Geoscience and Remote Sensing , vol. 51, no. 1, pp. 57-72, Jan. 2013.

Raney, R. K. , (2014) “Milestones in altimeter performance: Past, present, and future with relevance to coastal altimetry,” presented at the 8th Coastal Altimetry Workshop, Konstanz, Germany, Oct. 23/24, 2014

Ray, C.; Martin-Puig, C.; Clarizia, M.P.; Ruffini, G.; Dinardo, S.; Gommenginger, C.; Benveniste, J., "SAR Altimeter Backscattered Waveform Model," in IEEE Transactions on Geoscience and Remote Sensing, vol.53, no.2, pp.911-919, Feb. 2015.

Scagliola, M., M. Fornari and N. Tagliani, (2015) "Pitch Estimation for CryoSat by Analysis of Stacks of Single-Look Echoes," in IEEE Geoscience and Remote Sensing Letters , vol. 12, no. 7, pp. 1561-1565, July 2015.

Scagliola M., , M. Fornari, J. Bouffard, T. Parrinello, (2018) The CryoSat interferometer: End-to-end calibration and achievable performance, Advances in Space Research, Volume 62, Issue 6, 2018, Pages 1516-1525, ISSN 0273-1177